2012-04-18

Cavitation of a Water Jet in Water

Michael Marshall Wright
Brigham Young University - Provo

Cavitation of a Water Jet in Water

Michael M. Wright

A thesis submitted to the faculty of
Brigham Young University
in partial fulfillment of the requirements for the degree of

Master of Science

Tadd T. Truscott, Chair
Steven E. Gorrell
R. Daniel Maynes

Department of Mechanical Engineering

Brigham Young University

June 2012

ABSTRACT

Cavitation of a Water Jet in Water

Michael M. Wright
Department of Mechanical Engineering, BYU
Master of Science

Cavitation is a phenomenon that occurs in liquids when the pressure drops below the vapor pressure of the liquid. Previous research has verified that cavitation bubble collapse is a dynamic and destructive process. An understanding of the behavior of cavitation is necessary to implement this destructive mechanism from an axisymmetric jet for underwater material removal. This work investigates the influence of jet pressure and nozzle diameter on the behavior of a cloud of cavitation bubbles generated by a submerged high-pressure water jet. First, this investigation is put into context with a condensed historical background of cavitation research. Second, a description of the cavitation-generating apparatus is given. Next, the experimental methods used to explore the behavior of the cavitation clouds are explained. Finally, the results of the investigation, including propagation distance, cloud width and area, pulsation frequency, and cloud front velocity are presented. Among the results is a discussion of the significant experimental factors affecting the behavior of the cavitation clouds. It is shown that the Reynolds number, specifically the diameter of the nozzle, has a significant effect on the measurements. In some cases the jet pressure, and subsequent jet velocity, had a less significant effect than was expected. Overall, this research describes the cavitation cloud formed when a submerged high-speed water jet discharges.

Keywords: cavitation, submerged water jet, cavitation cloud, propagation distance, nozzle diameter, pulsation frequency, Reynolds number, front velocity

ACKNOWLEDGMENTS

I must first acknowledge Dr. Tadd Truscott for accepting me as one of his first graduate students. He has been incredibly supportive and helpful throughout my graduate studies. I am appreciative of my graduate committee for their support and direction. Kevin Cole and Ken Forster were instrumental in helping with data acquisition and part fabrication, respectively.

I am grateful for the Naval Research Enterprise Internship Program (NREIP) and Dr. David Beal at the Naval Undersea Warfare Center (NUWC) for the opportunity to spend an incredible summer working on this research in Rhode Island. I also thank Amanda Dropkin at the Naval Undersea Warfare Center for her collaboration on this project.

Finally, I express special thanks to my loving wife, Emily, and my son, Elliott, for their continual support.

TABLE OF CONTENTS

LIST OF TABLES

LIST OF FIGURES

NOMENCLATURE

σ	Cavitation number
P_o	Flow Pressure
P_v	Vapor Pressure
ρ	Density
V_j	Jet velocity
A_{inlet}	Pipe area
A_{exit}	Nozzle area
P	Pressure
z	Height
g	Gravity
f	Friction factor
L	Pipe length
D	Pipe diameter
K	Minor losses
$\wp$	Power
V_f	Front velocity
C_D	Coefficient of drag
A_{equiv}	Area of equivalent cavitator
A_j	Jet area
λ	Slenderness ratio
D_c	Cavity diameter
d_j	Jet diameter
L_{cavity}	Cavity length
Re	Reynolds number

CHAPTER 1. INTRODUCTION

The principle of cavitation has been a topic of research for well over a century. Damage to solid materials resulting from cavitation was first observed in the nineteenth century, but it was not until the twentieth century that a proper investigation was able to definitively claim that cavitation eroded solid materials in certain flow situations [1]. Research on cavitation continues today in a few principal areas. These areas include, but are not limited to: the composition and behavior of cavitation, methods to prevent or reduce the damage caused by cavitation, and techniques to take advantage of the cavitation phenomenon for mining, cleaning, etc. The aim of the work presented here is to quantify the observed behavior of cavitation from a water jet.

1.1 Objectives

This research examines the behavior of a cavitation cloud created when a high-pressure axisymmetric water jet is submerged in quiescent water. In spite of abundant research on various subtopics of cavitation, little research has been done in this particular area. Much of the available research surrounding cavitation deals with the interaction of cavities and solid surfaces, specifically, bubble formation and collapse near a solid surface, cavitation erosion, and methods to either incorporate or mitigate cavitation in real-world applications. Research shows that a surface can be damaged if cavitation occurs on or near it. Measurements of the geometry and performance of cavitation bubbles being transported downstream from an axisymmetric water jet are presented here.

When a high-pressure column of water is discharged through a small-diameter straight nozzle into quiescent water the accompanying drop in pressure from the accelerated column of water can result in the formation of cavitation bubbles. These vapor bubbles conglomerate into a cavitation cloud whose momentum carries the cloud away from the nozzle.

The objective of this work is to determine what happens to the cavitation cloud after it is emitted from the nozzle of the jet. Various experimental parameters including nozzle diameter and jet pressure are modified and the resulting effects on the cavitation cloud are recorded. High-speed photography and pressure instrumentation were the means of capturing the dynamic behavior of these events. From this data the relationship between nozzle diameter and jet pressure, specifically Reynolds number (Re), in regards to propagation distance, cloud width and area, pulsation frequency, and cloud front velocity was discovered.

The remainder of Chapter 1 describes some background information regarding cavitation. A few historical details are given on the discovery of cavitation. A brief description of the fluid mechanics of cavitation follows. Next is an outline of some pertinent contemporary research on cavitation. A section of theoretical calculations and expectations concludes the chapter. After the background is laid out, Chapter 2 introduces the experimental methods. Included here are descriptions of the design of the experimental apparatus, the instrumentation and data acquisition that was required, as well as information on the high-speed photography setup and image processing. The experimental results and discussion follow in Chapter 3. These results detail the behavior of the cavitation cloud for the various experimental parameters. Finally, Chapter 4 is a summary of the present and future work.

1.2 Background

Research on cavitation is plentiful. Prominent scientists from the past played major roles in the discovery of cavitation and our modern understanding of this phenomenon. This section introduces the first investigations into cavitation as well as descriptions of the fluid mechanics that govern it. Relevant contemporary research is then presented to introduce the study found in this thesis.

1.2.1 History

The term *cavitation* was first used to describe voids in liquid flows beginning in the late nineteenth century. The renowned Osbourne Reynolds [2], famous for the non-dimensional Reynolds number, performed "experiments showing the boiling of water in an open tube at ordinary temper-

atures" in 1894. In his experiments he forced water through a converging–diverging glass tube. In the throat of which, he noticed the formation of a small white cloud, and heard sounds similar to those heard when water in a kettle boils. The cloud was composed of vaporous voids resulting from the drop in pressure as the water accelerated through the throat of the nozzle.

Around the turn of the twentieth century hydromechanical systems—pumps, valves, propellers, etc.—were becoming more powerful and began showing curious signs of damage. The intensity of the damage was particularly unnerving on new, fast transatlantic steamers [3]. The rotational velocity of their propellers was greatly increased as these ships were designed with more powerful engines. The result being that the propellers were experiencing erosion problems almost immediately upon setting sail. In 1915, the Board of Invention and Research in London, formed a commission to determine the cause of this propeller damage [1].

This commission investigated five possible causes of the damage: metal surface structure, working stress, water impingement, cavitation, and water hammer. The first three possible causes were shown to not produce any pitting damage. The other two causes, cavitation and water hammer, showed the propensity to erode the propellers. The commission came to the conclusion that

> "cavitation will only produce erosion when accompanied by conditions which cause the cavities to collapse in such a way and in such a position that the energy of collapse is concentrated on a small portion of the propeller surface" [1].

It would be desirable to be able to predict and control the conditions that lead to erosion. The research herein presented tries to address this. One of the members of the commission, who was not a member of the Royal Society, S. S. Cook [4], was allowed to publish his contributions to the commission's study in 1928. He concluded that water droplets eroded the turbine blades by the water hammer effect; which can be described as high-pressure waves in a flow as a result of the flow being abruptly stopped by a solid or other obstruction. He also postulated that the velocity of the surface of a vapor cavity accelerates as the cavity collapses, which is related to the internal pressure of the cavity [4]. Rayleigh improved on Cook's theory by accounting for the compressibility of the vapor during the collapse of the cavity. These two results provide the basis for calculating the pressure developed by a collapsing cavitation bubble, and have been used by

many subsequent researchers to help explain how a simple vaporous cavity can transmit enough energy to erode strong materials like steel and rock.

1.2.2 Mechanics of Cavitation

Cavitation is a phenomenon that occurs in liquids, and depends on the non-dimensional Cavitation number σ reaching a flow-dependent critical value [5]. The critical value is reached when a liquid flow significantly increases velocity, or the pressure of the flowing fluid drops to the vapor pressure as described by:

$$\sigma = \frac{P_o - P_v}{\frac{1}{2}\rho V_j^2}; \tag{1.1}$$

where P_o defines the pressure of the flow, P_v is the vapor pressure, ρ is the fluid density, and V_j is the velocity of the flow [6]. The propensity for a flow to cavitate increases as σ nears zero. The type of flow, i.e. internal pipe flow, axisymmetric external flow, flow over a propeller, etc., determines how low σ must be before cavitation begins, there is no single value for σ below which cavitation is guaranteed and above which it is not possible. When σ nears the flow-specific critical value vapor cavities begin to emerge from nucleation sites, expand, and can coalesce into a cavitation cloud. As the velocity of the flow decreases, the pressure rises back above the vapor pressure and the cavities begin to collapse. From experiments performed by Wu and Chahine [7], the interior composition of coalesced cavities is primarily water vapor. The compressibility of the internal vapor results in high internal gas pressure that is inversely proportional to the radii of the cavities [4, 8]. Research presented by Ooi [9] demonstrates that the Cavitation number becomes less dependent on the Reynolds number of the flow as the flow velocity is increased. For his experiments this was confirmed in flows greater than 20 m/s. The water jets used in the current investigation are much faster than 20 m/s. Gopalan et al. [10] discuss the existence of vorticity and strain in the shear layer of an axisymmetric jet, which contributes to the inception of cavitation by lowering the local pressure. They, as well as O'Hern [11], show that cavitation inception occurs in the cores of streamwise vortices. Soyama et al. [12] show that a submerged water jet behaves significantly different than a water jet in air. The jet's shear layer exhibits considerable cavitation potential resulting in high erosion rates. For the current study an axisymmetric jet was used to

generate cavitation. The cavities appeared to form in the shear layer initially, until the rest of the jet would cavitate.

Once formed, cavitation bubbles are unstable and can break into smaller parts then reform back to their original shape [3]. The life of a gas bubble consists of many collapse and rebound episodes [13]. This result will be shown in subsequent sections. The frequency of an oscillating bubble is not affected by the shape of the bubble; however, the oscillation frequency can be reduced if the bubble is near a solid boundary [14]. Hutli and Nedeljkovic [15] have shown that the cavitation emitted from a submerged jet is periodic in nature. An axisymmetric cavitating jet pulses from the nozzle because of a reentrant jet at the tail end of the cavitation cloud [16]. Sato et al. [17] also show from high-speed photography that a chain-reaction of bubble collapses results from local collapses in the cavitation cloud that send a pressure wave through the flow. According to Hansson and Mørch [18], the cloud collapse begins at the periphery and moves inward. This work quantifies some of these behaviors.

1.2.3 Cavitation Erosion

Cavitation bubble collapse is a dynamic event [5] for which extensive research is available regarding the potential for cavitation bubbles to erode surfaces. It should be noted that this section describes the effects of single bubble interactions more than the interactions of clouds of bubbles. Cavitation erosion, or pitting, is the removal of surface material as a result of the remarkably destructive interaction of shockwaves and micro-jets. According to Reisman et al., "Bubbly shockwaves play a critical role in generating pressure pulses, which lead to cavitation noise and damage" [19]. The dynamic nature of the cavity collapse generates shockwaves, and if the collapse occurs near a solid boundary an extremely high-pressure micro-jet can impinge on the solid surface [20]. Considerable research shows that these shockwaves and micro-jets are strong enough to cause yielding and failure of solid materials [4, 20–24].

Coleman and Scott [21] present research showing submerged cavitating jets that exhibited varying erosion results for five metals, mostly aluminum alloys typically used in environments where cavitation can occur. They claim impinging jets deform the metal surfaces, which leads to ductile flow, tearing, and finally removal of the torn metal fragments. Bourne and Field [22] add that collapsing bubbles generate high-speed jets that impinge on the contact surface. The mecha-

nism of these impinging jets was further explained by Jayaprakash et al. [24] and Brujan et al. [23]. For a single bubble at a standoff distance between 0.9 and 1.1 (the ratio of distance from wall to maximum bubble radius) the spherical bubble becomes toroidal as a jet penetrates from the far side to the bubble-wall boundary. This torus subsequently breaks up into several spherical bubbles that also impinge on the boundary. These smaller bubbles have increasingly higher pressures [4, 8] that result in even faster jet impingement. Annular erosion patterns are common in single cavitation bubble applications and this torus explanation clarifies why this pattern occurs [20, 21, 23]. On a macro-scale, annular patterns are also common, but this is from the fact that most of the cavitation forms in the shear layer of the jet [10–12].

Philipp and Lauterborn [20] show that three effects of single bubble collapse lead to cavitation erosion. First, a shock wave generated upon bubble collapse increases the local pressure. Second, the impinging liquid jet exerts high pressures on the surface. Finally, during collapse the bubble is drawn closer to the surface increasing the potential damage from either the first or second effect. One practical application of these cavitation principles was shown by Lu et al. [25], where laser-drilled holes in metal plates underwater were cleaner than laser-drilled holes in plates in air. Micro-jets from the cavitation bubble collapse that were formed by a laser heating the water impacted their metal specimens with much higher forces than laser ablation alone.

1.3 Theoretical Approach

Before any experiments were performed it was necessary to make a few theoretical predictions of what would occur. One application using high-speed jets in a submerged environment that has been rigorously studied is the use of a jet to form a supercavity around a submerged torpedo. Unclassified defense documents outline some of this work, which provided a starting place for predictions of the behavior of the cavitation in this study.

Without being able to measure the nozzle exit velocity a theoretical prediction based on standard fluid flow in a pipe was made [6]. A predicted jet velocity is necessary to predict σ, which is used in predicting the cavity geometry. The theoretical jet velocity is:

$$V_j = \frac{A_{inlet}}{A_{exit}} \sqrt{\frac{2\left(P_{inlet} - P_{exit}\right) + \rho g\left(z_{inlet} - z_{exit}\right)}{\rho\left(\left(\frac{A_{inlet}}{A_{exit}}\right)^2 + \frac{fL}{D} + \left(\frac{A_{inlet}}{A_{exit}}\right)^2 \Sigma K - 1\right)}}; \tag{1.2}$$

where A_{inlet} is the area of the pipe, A_{exit} is the area of the nozzle exit, P_{inlet} is the reservoir pressure, P_{exit} is the quiescent water pressure, g is gravity, z_{inlet} and z_{exit} are the relative heights of the reservoir and nozzle, f is the friction factor for stainless steel pipe, L is the length of the pipe, D is the pipe diameter, and ΣK is the sum of all minor losses, such as bends and constrictions, in the system. This is the velocity used in Equation 1.1 to predict whether or not the flow will cavitate.

The formation of cavitation from a high-speed jet in quiescent water can be mathematically modeled as cavitation formed by a disk cavitator in a moving flow [26]. A comparison between the power of the cavity front ($\wp_{out}$) to the power of the jet ($\wp_{in}$) is made to determine the front velocity of the cavity generated by the high-speed jet. These are given by:

$$\wp_{out} = \frac{1}{2}\rho V_f^2 A_{equiv} C_D V_f; \tag{1.3}$$

$$\wp_{in} = \frac{1}{2}\rho (V_j - V_f)^2 A_j (V_j - V_f); \tag{1.4}$$

where ρ is the density of the water, V_f is the front velocity, V_j is the jet velocity, A_{equiv} is the equivalent area of the cavitator, and A_j is the area of the jet. $C_D = 0.82$, which is the coefficient of drag for a disk cavitator as given by Savchenko [27]. Equating Equations 1.3 and 1.4 and solving for the front velocity gives:

$$V_f = \frac{V_j}{1 + \left(\frac{A_{equiv} C_D}{A_j}\right)^{1/3}}. \tag{1.5}$$

The geometry of the cavity modeled as if generated by a disk cavitator can be described as a function of σ given by May [26]:

$$\lambda = \frac{L}{d} = 1.067\sigma^{-0.658} - 0.52\sigma^{0.465} \tag{1.6}$$

where λ is the slenderness ratio, L is the length of the cavity, d is the diameter of the widest part of the cavity. The cavity diameter can be determined from the jet diameter, d_j, according to May [26] by:

$$D_c = \frac{d_j}{0.205}\sqrt{\frac{C_D}{\sigma}}. \tag{1.7}$$

The length of the cavity is found from λ and D_c, as:

$$L_{cavity} = \lambda D_c. \tag{1.8}$$

Using the experimental parameters discussed later in Chapter 2, theoretical values were calculated for Equations 1.1–1.8. The jet velocity was predicted to range from 100 m/s to about 130 m/s. From these velocities the range of σ was from 0.0201 at low jet velocity down to 0.0124 at the highest jet velocity. The predicted cloud front velocities were only between 27 m/s and 35 m/s, and theoretical propagation lengths extend from 0.30 m as far as 1.5 m downstream. These theoretical calculations will be compared to experimental values in Chapter 3.

1.4 Conclusion

This chapter introduced cavitation by giving a short history of its discovery, describing the fluid mechanics that govern the formation of cavitation, and presenting previous studies of cavitation behavior. The erosive capabilities of cavitation have clearly been established. The final section outlined a theoretical approach to determining cavitation behavior as a function of the size and velocity of the initial water jet. The research to be presented expands on the behavior of cavitation clouds already described. Some interesting relationships between jet size and pressure will be described, and comparisons between predicted and measured cavitation behavior will be given.

CHAPTER 2. EXPERIMENTAL METHODS

This chapter describes the experimental setup and parameters used in the study of cavitation cloud behavior. The design and operation of the water jet apparatus is explained first. Next is a description of the instrumentation and data acquisition used in the experiments. Lastly, a section is devoted to the high-speed photography and image processing techniques used in this study.

2.1 Experimental Setup

This section illustrates the design of the water jet. The jet device and the full test setup are described in detail. The peculiarities of the design are clarified and justified. Security measures to prevent injury were in place during all testing. The extremely high-pressure gas used in the experiment required all components to be rated for such pressures. The entire experiment was done in a lockable room, and warning signs were used to prevent accidents due to tampering. Proper safety equipment, including eye protection, was required of all persons in the room during the experiments.

2.1.1 Experimental Configuration

In the literature on cavitation there have been various methods of cavitation generation. The method adapted to this experiment used high-pressure gas to accelerate a column of water through a nozzle with sufficient velocity that the resulting jet cavitated. This method created a single shot or discharge of the jet that lasted only as long as it took to discharge the fixed volume of water; it was not a continuous stream. A layout of the experimental setup is shown in Figure 2.1. The main components of the setup were the jet, a rigid frame onto which the jet was mounted, and a tank of quiescent water. In addition to these components there was electronic instrumentation, including power supplies, a high-speed camera, pressure transducers, and a computer to which the electronics were connected.

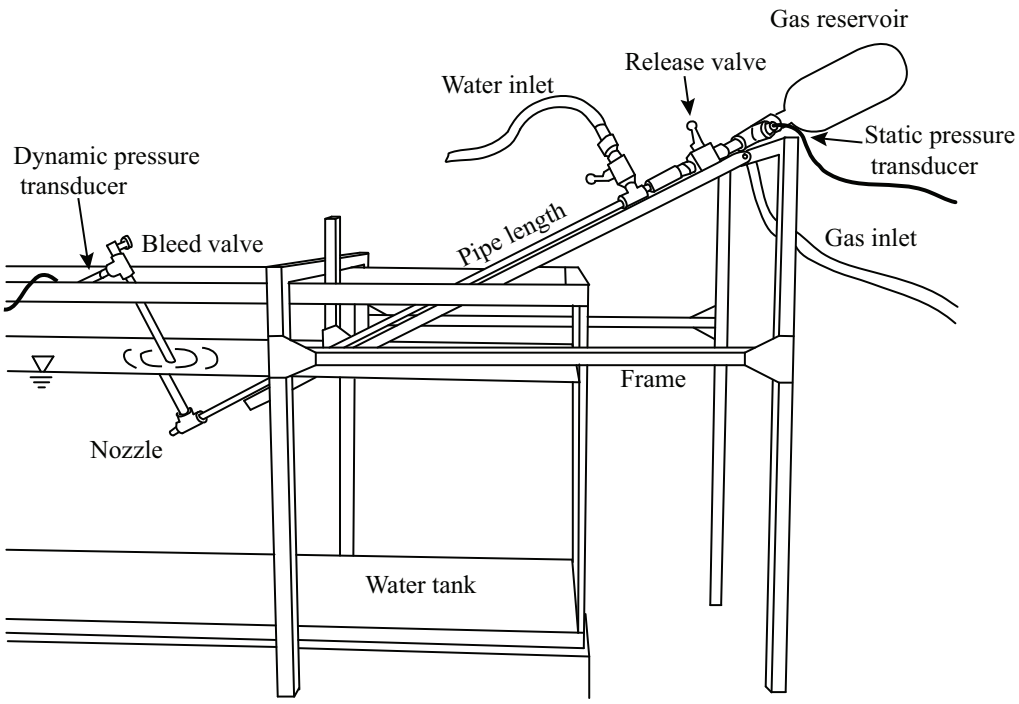

Figure 2.1: Experimental test setup showing the jet apparatus mounted on a frame to be discharged into a water tank. The water inlet hose, compressed gas inlet hose, and pressure transducers are also visible.

The water tank was made of glass and measured 1.83m$\times$0.61m$\times$0.61m. A rigid framework of 2.54 cm square extruded aluminum surrounded the tank to which the jet was affixed. The framework was fixed to the floor to prevent movement when the jet discharged. The nature of the jet and tank configuration required that the jet be mounted at an angle below horizontal. Full adjustability of the framework allowed the jet to be aligned at various angles. The decline also ensured that the water column was fully discharged through the nozzle without the pressurized gas simply passing over the top of the water in the pipe. Figure 2.2 shows the difference between the cavitating jet and pure gas exiting the nozzle at the end of the jet discharge. It is unlikely that this particular jet could be feasibly used in a horizontal position due to the possibility for the pressurized gas to escape without discharging the water. Additionally, to eliminate the possibility of air being entrained in the jet from the surface it was requisite that the nozzle be at a sufficient depth in the tank of water. This depth was approximately 20 cm, and throughout the experiments no air entrainment was observed.

(a) Cavitating water jet: 1.0 mm nozzle, 20.7 MPa

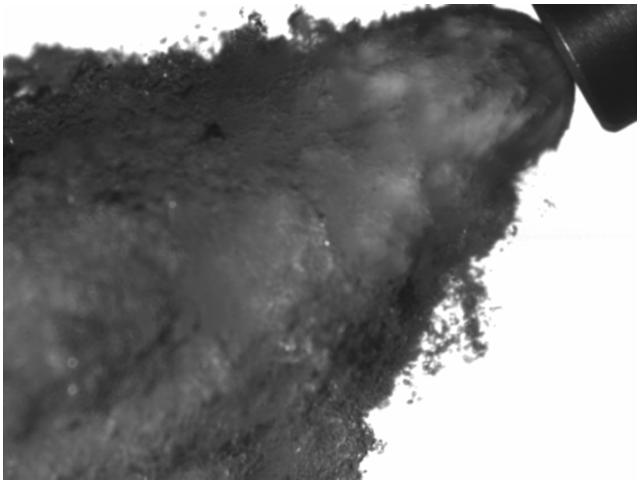

(b) Gas exiting nozzle after jet discharge

Figure 2.2: Comparison between cavitating water jet and gas following the jet discharge. (a) Cavitation bubbles move away from the nozzle without expanding much. (b) The pressurized gas expands rapidly upon exit after discharging all of the water.

2.1.2 Water Jet Design

The jet apparatus consisted of a series of valves and pipes. These valves separated a reservoir of ultrahigh-pressure nitrogen (nitrogen was chosen for its inert properties and availability at ultrahigh pressure) from a length of pipe filled with tap water at the end of which was a small-diameter orifice nozzle. Figure 2.3 shows the valve arrangement. A tank of ultrahigh-pressure nitrogen at 40 MPa was regulated into a smaller storage reservoir at the desired test pressure. The reservoir was a 1.15-liter carbon-fiber-wrapped paintball cylinder rated for 31 MPa. Test pressures

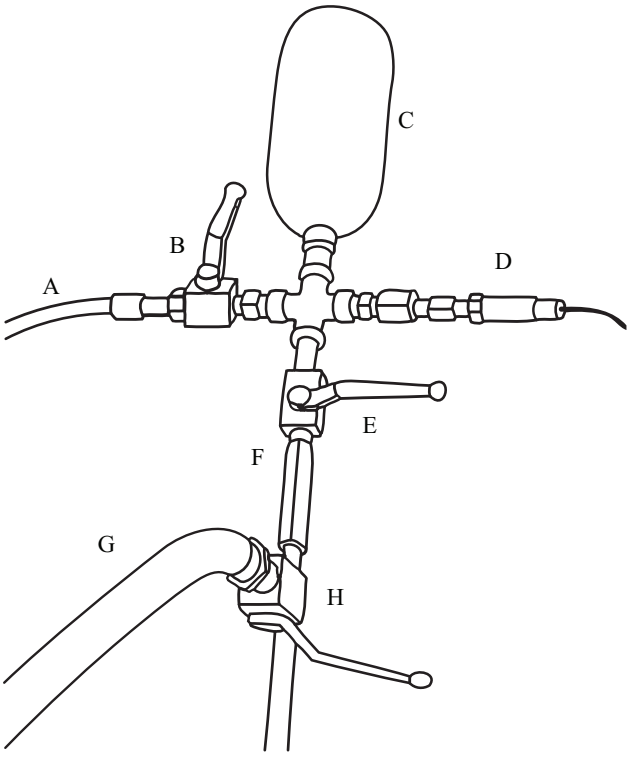

Figure 2.3: Water jet valve configuration. High-pressure nitrogen (A) fills reservoir (C) through valve (B) where a transducer (D) measures the static pressure. Check valve (F) separates the gas from water filled through valve (H) by hose (G). Opening valve (E) releases the gas to discharge the water.

never exceeded 28 MPa. Tap water filled a length of 6.35 mm diameter pipe through a separate port. A high-pressure ball valve and check valve separated the pressurized nitrogen from the pipe filled with water. The check valve was instrumental in preventing water from contaminating the gas reservoir. One of three standard zero-degree-spray-angle pressure washer nozzles was attached to the end of the length of pipe to create the water jet. Figure 2.4 illustrates the geometry of the nozzles. The length of the throat increased with increased diameter from 3.0 mm in the 0.7 mm diameter nozzle up to 3.4 mm and 4.5 mm in the 1.0 mm and 2.0 mm diameter nozzles, respectively.

All of the components that would be in contact with water were made of stainless steel to prevent corrosion. The mating connector between the small reservoir and the jet had to be custom fabricated out of high-strength carbon steel because the thread size of the small reservoir was not standard. The entire system was designed to withstand pressures up to 31 MPa, slightly greater than the maximum pressure to be tested. The weakest component had a factor of safety of 1.13.

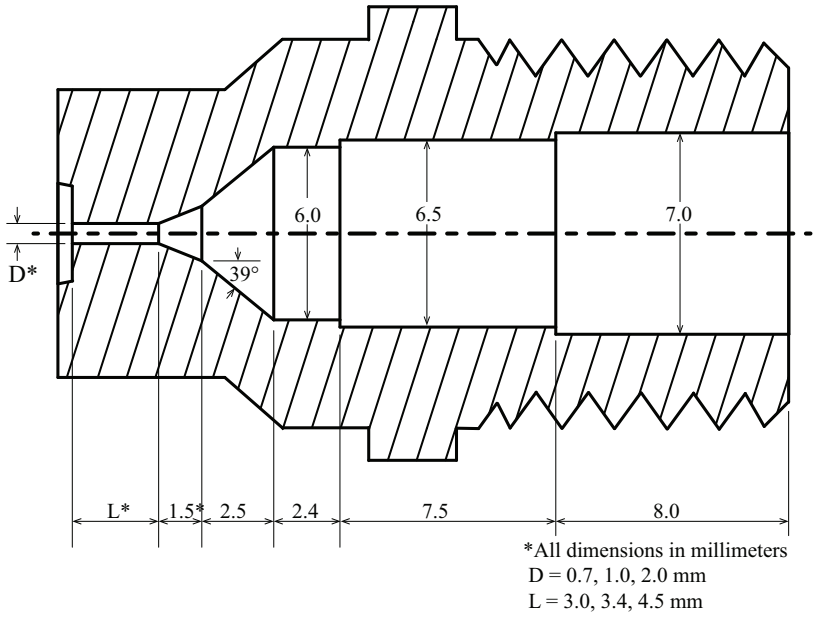

Figure 2.4: Geometry of the zero-degree-spray-angle nozzles used in the experiments. The length of the throat of the nozzle increased with increased diameter. For 0.7 mm diameter, length was 3.0mm. For 1.0 mm diameter, length was 3.4 mm. For 2.0 mm diameter, length was 4.5 mm.

2.1.3 Experimental Variables

Experiments were performed for a series of nozzle diameters, reservoir pressures, and water column lengths as a way to compare the effect each of these parameter had on the behavior of the cavitation. Table 2.1 outlines these experimental parameters. Various constraints on the pressurized gas and material sizes led to the particular parameters shown in Table 2.1. Nitrogen was chosen as the pressurized gas because of its inert properties. It is commercially available at a maximum of 41.4 MPa, which constrained the experimental pressures to be less than this maximum. The maximum test pressure of 27.6 MPa was chosen to provide a factor of safety greater than 1.0 for the entire device as previously described. The three nozzle sizes were the three smallest diameter nozzles that were easily compatible with the apparatus design and not cost-prohibitive. Preliminary calculations, as described in Chapter 1, predicted σ = 0.0124–0.020, which provided support that the jet using the chosen parameters would lead to cavitation. The Reynolds numbers of the jet, $Re = \rho VD/\mu$, with the given parameters are outlined in Table 2.2.

The primary data set of 36 tests (three tests for each nozzle at each of four pressures) was collected for the 0.45 m pipe. Initial experiments exhibited pulsation, which was believed to be

dependent on the pipe length. It was assumed that the longer pipes would affect the pulsation of the cloud; the results of which are explained in the next chapter. The other two pipe lengths provided comparisons to the primary data.

Table 2.1: Experimental Parameters

Pipe Length (m)	Nozzle Diameter (mm)	Reservoir Pressure (MPa)
0.45	0.7, 1.0, 2.0	17.2, 20.7, 24.1, 27.6
0.61	1.0, 2.0	17.2, 20.7, 24.1, 27.6
0.91	1.0, 2.0	17.2, 20.7, 24.1, 27.6

Table 2.2: Reynolds Numbers of Experimental Parameters

Nozzle Diameter	Pipe Length	Reynolds number			
		17.2 MPa	20.7 MPa	24.1 MPa	27.6 MPa
0.7 mm	0.45 m	63,000	70,000	75,000	80,000
1.0 mm	0.45 m 0.61 m 0.91 m	90,000	99,000	107,000	114,000
2.0 mm	0.45 m 0.61 m 0.91 m	181,000	198,000	214,000	229,000

2.2 Operation

This section describes the operating procedure of the jet to generate cavitation (refer to Figure 2.3). The procedure for discharging the water jet is as follows:

1. With all valves closed, open valve (B) separating the nitrogen tank from the reservoir (C)
2. Release nitrogen through the regulator to fill the reservoir, then close the separating valve
3. Fill the pipe with water through valve (H), and bleed off excess gas through the bleed valve near the nozzle (not shown in the figure)

4. With the data acquisition programs running and the camera ready, trigger the camera

5. Immediately after triggering the camera open the main release valve (E)

6. Close the release valve as soon as the jet fully discharges

This procedure was performed for each nozzle diameter at each of the four experimental pressures. The nozzle could be easily changed by unscrewing it and screwing in the next size without moving the apparatus, which was firmly fixed to the aluminum frame. After the initial 36 experiments the length of pipe for the water column was replaced by a longer pipe. In order to exchange this pipe the entire jet was removed from the frame and the pipe replaced. The jet angle changed slightly for the longer pipes, but this did not affect the experiments.

2.3 Instrumentation and Data Acquisition

Pressure instrumentation inside the jet allowed for precise pressure measurements to be made throughout each run. An Omega PX309-7.5KG5V static pressure transducer was connected to the pressurized reservoir to determine the test pressure. A pressure snubber, a connector consisting of a network of tiny passageways, separated the reservoir from the transducer to prevent pressure spikes that could damage the sensitive transducer diaphragm.

Knowing the pressure at the nozzle exit was necessary to compare experimental data with theoretical values. An Omega DPX101-5K dynamic pressure transducer with a resonant frequency of 500 kHz was used to measure this pressure. The transducer was connected just upstream of the nozzle by an extension of pipe. The length of pipe extended the transducer out of the tank of water since it was not waterproof (refer to Figure 2.1).

The pressure transducers each output a voltage signal between 0–5 volts. They were calibrated to produce 97 mV/MPa and 168 mV/MPa for the static and dynamic transducers, respectively. The uncertainty of the static transducer measurements was approximately ± 1.1 MPa, and the uncertainty for the dynamic transducer was approximately ± 0.5 MPa [28]. A schematic showing how the transducers and camera are connected to the computer is shown in Figure 2.5. The static and dynamic pressure transducers were powered separately by power supplies. The camera output two signals, one for the trigger and one for the shutter. The trigger signal was a positive

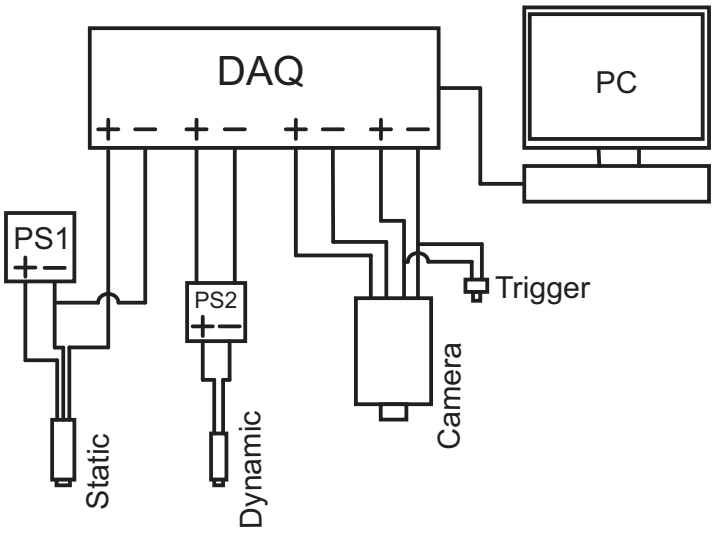

Figure 2.5: Data acquisition from transducers and camera to the computer. Both the static and dynamic transducer were powered by individual power supplies. Their output signal was routed into a data acquisition bus with two signals from the high-speed camera. The combined signals were read into a computer for further analysis.

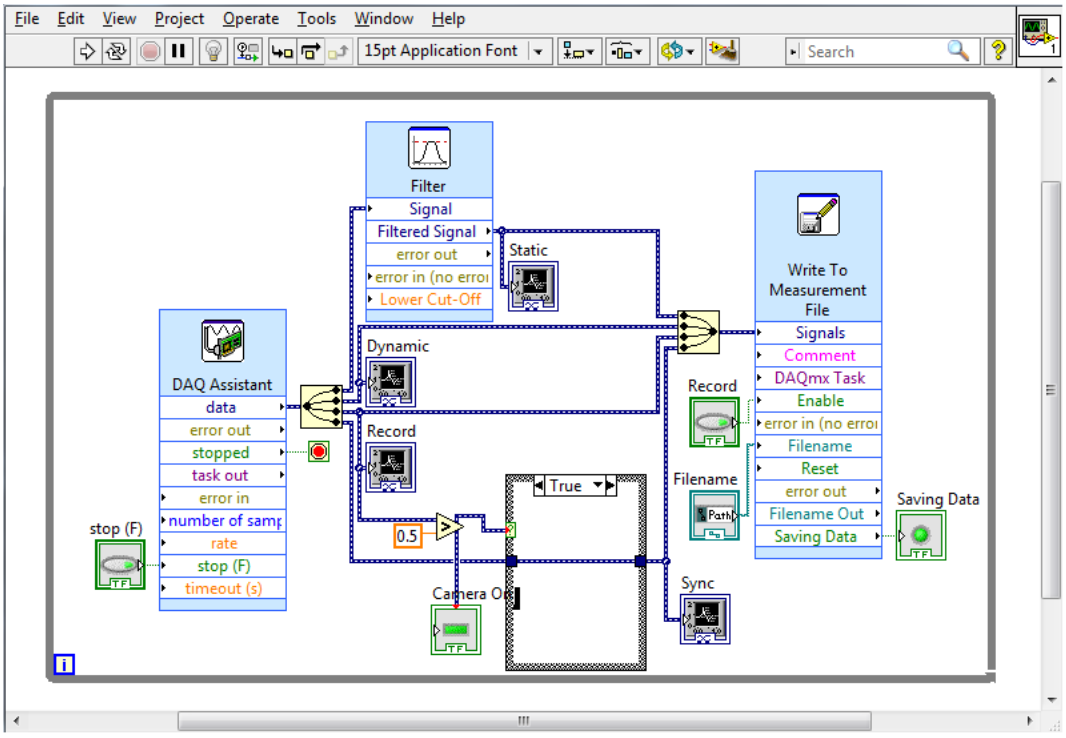

Figure 2.6: LabVIEW™ program block diagram showing how the four signals are read and stored in the computer for further analysis.

five volts beginning at the moment the trigger was depressed, and continued for the duration of the filming. The second camera signal was a pulse of five volts each time an image frame was recorded. This allowed for images to be correlated exactly to the pressure data. The four voltage signals, two from the transducers and two from the camera, were converted to digital signals to be analyzed in the computer.

The analog voltage signals from the pressure transducers and camera were converted to digital values by a NI USB-6211 DAQ and read into a LabVIEW™ program. See Figure 2.6. Data acquisition was set at 21 kHz in this program. This sampling rate reduced the likelihood of aliasing the five volt pulsed signal.

2.4 High-speed Photography and Image Processing

High-speed photography was the primary method of analyzing the cavitation behavior. For this investigation a single high-speed Photron SA-3 camera, whose frame rate was fixed at 5000 fps with shutter speed of 1/10000 s, provided clear flow visualization. There was still slight motion blur with these camera settings near the nozzle exit where the velocity was greatest. At this frame rate the recorded images had a maximum resolution of 768×128 pixels. To ensure that the entire cavitation cloud would be captured in each image frame the camera was rotated to the same angle as the jet. All images presented in figures here are horizontal, but it should be kept in mind that the jet was actually angled downward.

MATLAB® was used to process the high-speed images from which the overall propagation distance, cloud width and area, cloud frontal velocity, and pulsation frequency were computed. All of the scripts used are included in Appendix A.2. To be able to measure the geometry of the cavitation in the images, image calibration was necessary to convert measurements from pixels to centimeters. With the camera in position an image of a ruler with a centimeter scale in the water tank near the nozzle provided this relationship. Many pairs of points in the calibration image were chosen with the two points in each pair separated by one centimeter on the imaged ruler. The average number of pixels between each pair of points became the pixel-to-centimeter conversion factor. Table 2.3 summarizes the conversions used for the various configurations. The camera position had to be changed throughout the experiments as the cavitation cloud propagated out of

Table 2.3: Image Calibration Conversion Factors

Configuration	Conversion (pixels/cm)
0.45m (17.2-20.7 MPa) all nozzles	25.02
0.45m (24.1-27.6 MPa) 2.0 mm nozzle	20.7
0.61m all pressures and nozzles	19.5
0.91m all pressures and nozzles	19.25

the image frame. Each new camera position required a new pixel-to-centimeter conversion factor that was determined by the method described.

The propagation distance was measured from the nozzle exit to the location where the cavitation cloud collapsed. The pulses of each run collapsed at a parameter-specific common location. This process converted the distance between two manually chosen points in an image from pixels to centimeters. The chosen points were the stationary nozzle and the point of general collapse. The same procedure was used for the cloud width, except the points were measured at the upper and lower cloud edges.

To find the area of the cavities a more rigorous image processing approach was necessary. In order to find the area the images were converted into binary images. To accurately convert the many shades of gray into either black or white each image went through multiple processes. The nozzle was first eliminated from each image. Next, the background of each image was turned white using a disk structuring element five pixels in size. At this point the image was converted to a black jet on a white background. After inverting the black and white to get a white jet on a black background, the *bwarea* function was used to measure the area of each cavitation cloud. Figure 2.7 shows a raw image and the processed image from which the area was calculated. The white area bordered in red is the area that was measured.

To compute the cloud front velocity many sets of consecutive images were used. Three sets of multiple consecutive images were chosen from each run and two points were manually chosen in each image—one at the nozzle and the other at the cloud front just before the cloud collapsed. The change in front position between consecutive images gave the distance traveled between frames. The velocity was then calculated by dividing this distance by the known frame-separation time (0.0002 s).

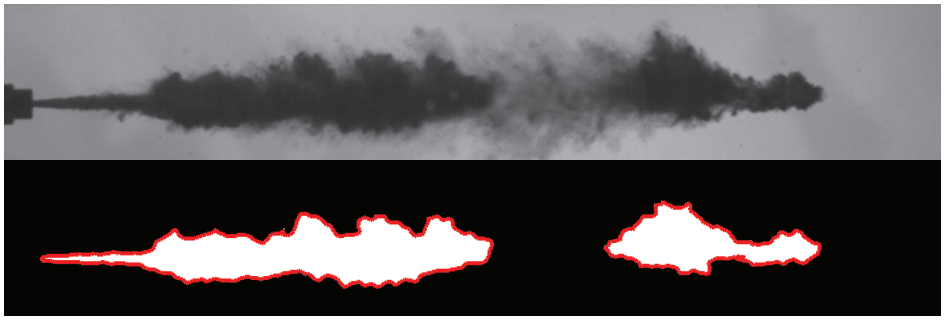

Figure 2.7: Cavitation cloud area measured from an image. Only the darkest parts of the image corresponding to definite cavities are measured. The red outline shows what area was measured.

Figure 2.8: Representative image of how the intensity of a single column of pixels (white line) at a fixed distance downstream from the nozzle is used to measure the frequency of pulsation.

The frequency at which each jet pulsed was determined using each image of the individual runs. The average color intensity of one column of pixels was measured at a fixed distance from the nozzle (see Figure 2.8). This intensity was measured at the same position for each image over the entire discharge of the jet. The intensity of the pixel column fluctuated according to the cloud pulsation (see Figure 2.9). A passing pulse was wider and darker which resulted in an average intensity closer to the value for total black. When the intensity values over the life of the cavitation were plotted the result was what appeared to be a noisy signal. Each discharge resulted in approximately 700 data points for the 0.7 mm diameter jet down to only approximately 250 data points for the 2.0 mm diameter jet. A Fast Fourier Transform (FFT) was used to find the component frequencies of the noisy signal. To give better results the data for each run was concatenated with itself three times (see Figure 2.9) before being run through the FFT. MATLAB's *fft* command was used to find the frequency spectrum of the intensity variation at this vertical segment of each discharge.

The most prominent frequencies of each run were plotted with those of the other runs, see Chapter 3. Figure 2.10 shows the resulting frequency spectrum of the data from Figure 2.9. There is an obvious peak between 500–1000 Hz. From this example, the frequencies of the three highest

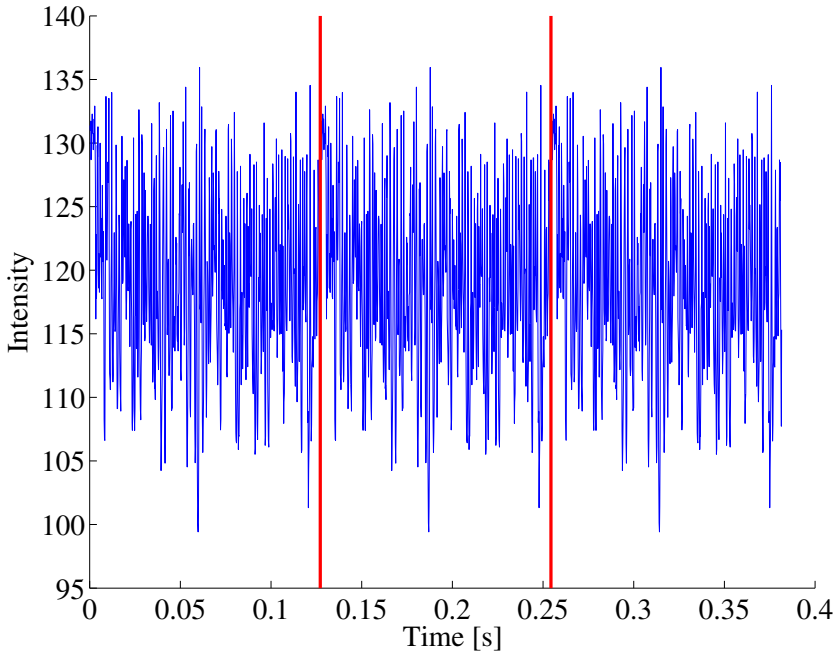

Figure 2.9: Concatenated intensity values for each image over the life of a jet at 20.7 MPa from the 0.45 m pipe and 1.0 mm diameter nozzle (Re = 99,000).

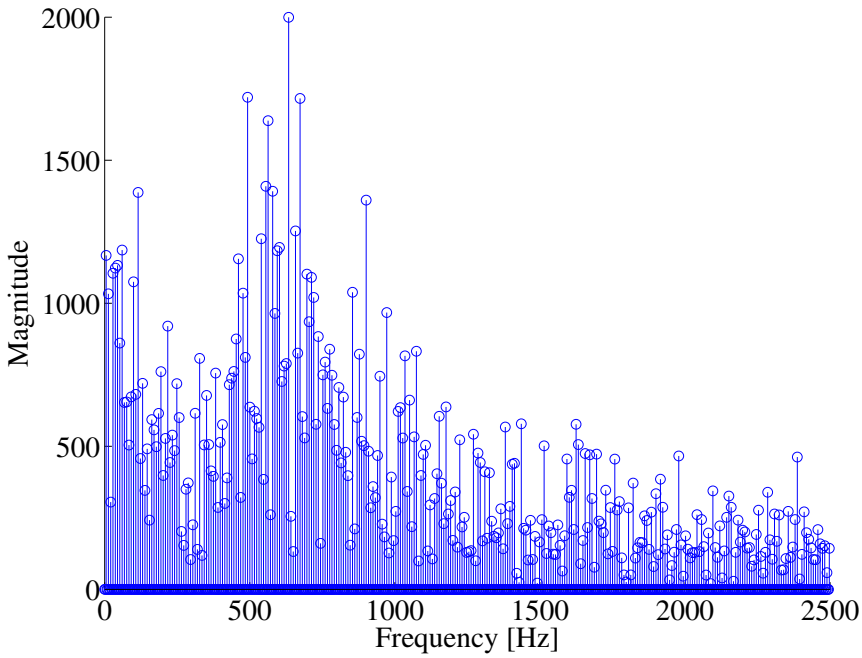

Figure 2.10: Example of the frequency spectrum of the measured intensity for a jet at 20.7 MPa from the 0.45 m pipe and 1.0 mm diameter nozzle (Re = 99,000).

peaks would be recorded. After doing this process for every experimental run the many data are plotted to visualize any frequency trends. In the next chapter, all of the cavitation measurements are presented with their associated uncertainties as calculated in Appendices A.1 and A.2.

2.5 Conclusion

This chapter described the experimental methods used to investigate the behavior of cavitation clouds from an axisymmetric water jet. The experimental configuration and water jet design were explained, as well as the operating procedure. The experimental variables—nozzle diameter, jet pressure, and pipe length—were given, including the reasoning of why they were chosen. Explanations of the pressure instrumentation, data acquisition, and high-speed photography were given to clarify how the experimental results were obtained. The remainder of this thesis presents the findings of the investigation.

CHAPTER 3. EXPERIMENTAL RESULTS AND DISCUSSION

This chapter presents a discussion of cavitation cloud behavior. The results are divided into sections—cavitation duration, propagation distance, cloud width, cloud area, pulsation frequency, and cloud front velocity. The principal case against which other cases are compared was for the 0.45 m pipe, 1.0 mm nozzle, at 20.7 MPa. Though all of the tested cases are included in the plotted data, only the most significant are illustrated in figures.

3.1 Experimental Results

A representative display of the cavitating jet is shown in Figure 3.1 for cavitation from the 0.45 m pipe length, 1.0 mm nozzle, at 20.7 MPa. The images reveal that the event was a cloud of small bubbles rather than a single supercavity. If the cavitation had been a single cavity the imaging technique of backlighting would have shown the translucence of the cavity. The apparent turbulent nature of the cavitation cloud and its opacity tend to suggest that the cavitation is a cloud of small bubbles. There is the possibility that a larger cavity exists inside the bubble cloud, but that is impossible to determine from these images. Savchenko [27] reported that in tests where a continuous water jet was used to generate a single supercavity supplementary, or artificial, gas injection was necessary for velocities less than 100 m/s. This means that at lower velocities no single cavity was formed without adding gas to the cavitation vapor pockets. The current tests all had predicted jet velocities greater than 100 m/s, but the streams were not steady. This unsteadiness could explain why no supercavities were formed. For all of the tests the cavitation cloud formed at the nozzle, propagated downstream, and collapsed.

The first column of Figure 3.1 shows the initial formation of a cavitation cloud. The first, middle, and last frame of each column shows the time from when the first cavitation bubbles were visible. The time step between each frame is $\Delta t = 0.0004$ s. The other two columns of the figure are sequences of the same jet from later times. Throughout the discharge every run exhibited pulsation.

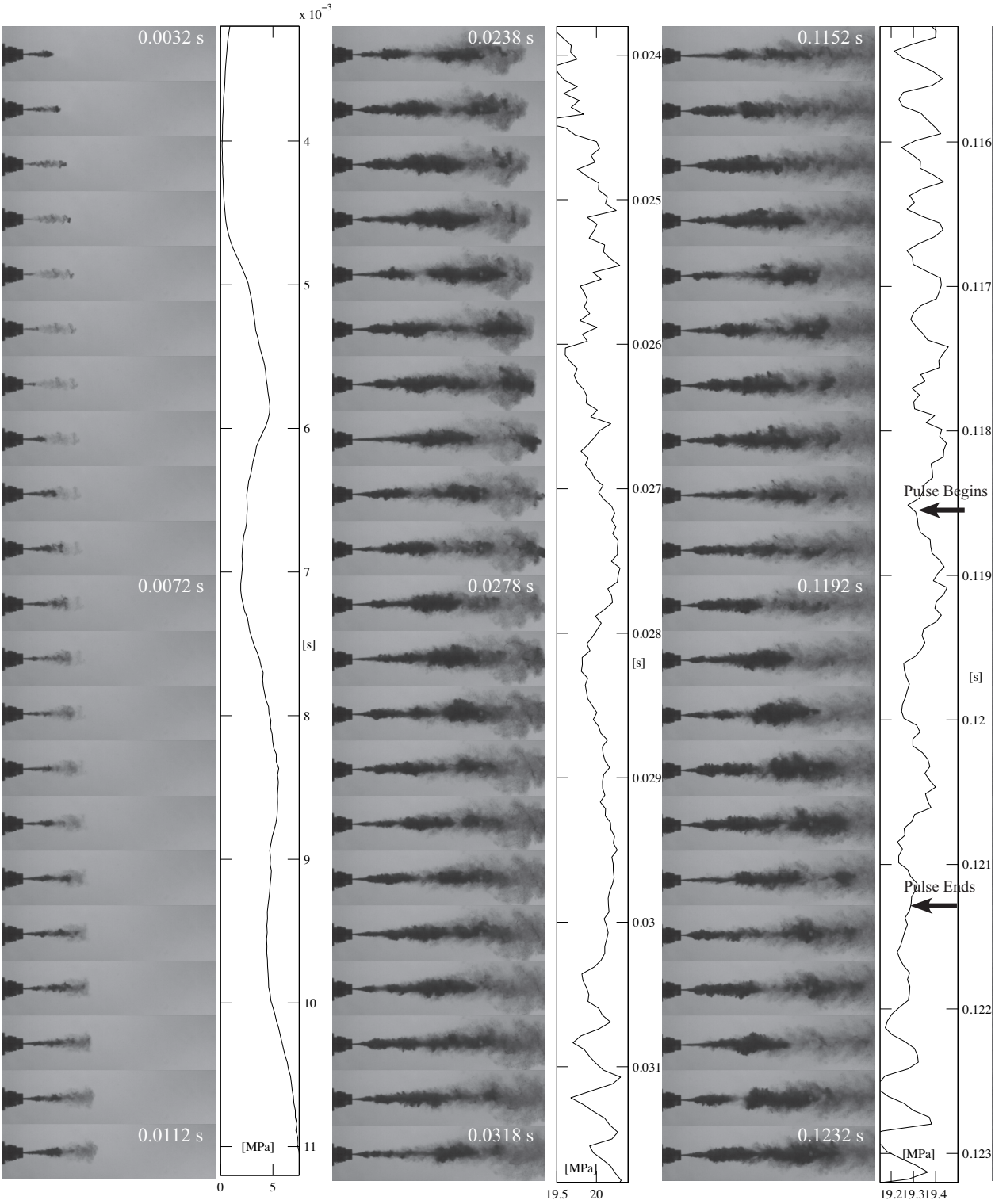

Figure 3.1: Image sequence with a Δt=0.0004 s of three time periods of a cavitating water jet from a 0.45 m long pipe with a 1.0 mm nozzle at 20.7 MPa (Re = 99,000). Time stamps show the time from cavitation inception. The cavitation is formed at the nozzle, moves downstream as a cloud, and collapses. The nozzle exit pressure as a function of time plotted to the right of each sequence shows jet pulsation (Frame rate: 5000; shutter: 1/10000 s; resolution: 768×128).

The sequence shows how a pulse of cavitation bubbles traveled from the nozzle downstream and collapsed at a certain distance. See Figure 3.1, column 2, frames 1-9. In column 2, frame 1, near the nozzle a pulse begins. It is seen to grow longitudinally as well as axially. The pulse continues to grow until the cloud separates from the nozzle and a new pulse begins. The fifth frame of column 2 shows another pulse beginning before the previous pulse fully collapses. In frame 9 the pulse that began in frame 1 finally collapses.

Along the vertical axis of each column of images, a pressure plot from the nozzle exit shows that the pressure inside the pipe was unsteady. This unsteady effect caused the jet pulsation from the nozzle. The collapse and rebound of the bubbles in the free stream was the result of a different phenomenon related to gas bubbles in liquid (see [13, 14]). The mass collapse occurred as described in Chapter 1, where individual bubbles collapse on the periphery of the cloud sending pressure waves through the cloud. These waves cause more individual bubbles to collapse until the entire cloud collapses. See [17, 18] for further reading on this. It is sufficient for this research that the cloud of bubbles collapsed at a common location based on the experimental parameters. Pulses from the image sequences can be correlated with the pressure plots. For example, in the third column of Figure 3.1 a new pulse is seen in the eleventh frame from the top (t = 0.1192 s) and a pressure increase begins just before this time (about 0.1186 s), as marked in the pressure plot. Since the new pulse is already far away from the nozzle in frame 11, it can be assumed that this pulse began around 0.1186 s because of the pressure surge, before it is seen at 0.1192 s. Additionally, it appears that a decrease in pressure registered on the plots corresponded to the cavitation cloud moving away from the nozzle just before a new pulse begins. Before the pulse that began around 0.1186 s moves downstream and collapses (see arrows in Figure 3.1), there are two additional pulses. The first new pulse occurs around 0.12 s, and is visible in frame 13. The second new pulse begins around 0.121 s and is visible in frame 16 just as the original pulse that began in frame 11 finally collapses.

Figure 3.2 plots the pressure of the full cavitation sequence for the 1.0 mm diameter nozzle at 20.7 MPa (Re = 99,000) from Figure 3.1. The dashed lines outline which portions of the full test are shown in the image sequences. The leftmost pair of lines is for the first column of Figure 3.1, and it can be seen that the pressure is ramping up. The center pair of lines is for the center column just as the pressure reaches a plateau. The rightmost pair of lines separates the third column near

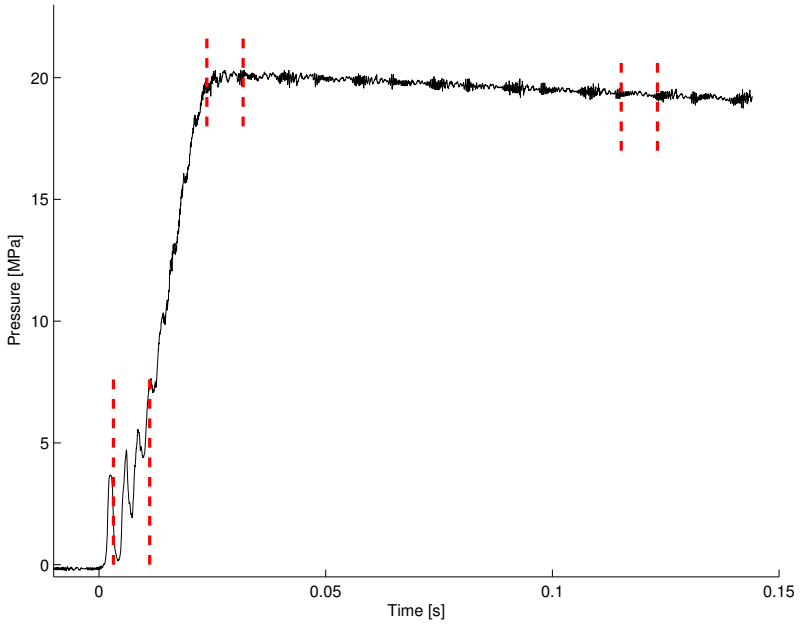

Figure 3.2: Pressure–time plot for Figure 3.1. The leftmost pair of lines delineates the pressure corresponding to the first column of Figure 3.1. The center pair of lines is for the center column of Figure 3.1. The rightmost pair of lines if for the third column of Figure 3.1 near the end of the life of the jet.

the end of the life of the jet. The pressure oscillated during the discharge of each jet as seen for one run in Figure 3.2.

Figures 3.3, 3.4, 3.6, 3.7, and 3.8 also show the formation and general tendencies of cavitation from the 0.45 m pipe with varied pressure and nozzle diameter. Figure 3.3 shows cavitation from the 1.0 mm nozzle at 17.2 MPa (Re = 90,000). Figure 3.4 shows cavitation from the same nozzle at 24.1 MPa (Re = 107,000). Figure 3.6 shows cavitation again from the same nozzle at 27.6 MPa (Re = 114,000). Figure 3.7 shows cavitation from the 0.7 mm nozzle at 20.7 MPa (Re = 70,000). Figure 3.8 shows cavitation from the 2.0 mm nozzle at 20.7 MPa (Re = 198,000). These image sequences illustrate the cavitation cloud behavior for varied pressure and varied jet diameter.

Figure 3.3 illustrates the initialization of a cloud from the 1.0 mm nozzle and 0.45 m pipe at 17.2 MPa. The frame separation time for this and the following two sequences (Figures 3.4 and 3.6) is Δt=0.0002 s. The first column shows that a small pulse exits the nozzle and quickly collapses. The pressure plot on the vertical axis shows how the pressure increases from near zero

to 5 MPa in a very short time (0.0042 s). Once the full pressure stabilizes somewhat, columns 2 and 3 show that only minor pressure fluctuations are present. These fluctuations are still large enough to cause the jet to pulsate though. The image sequence shows the growth and collapse of the cavitation cloud.

It can be seen in Figure 3.4 that for the same size nozzle, 1.0 mm, at higher pressure, 24.1 MPa, (Re = 107,000) the cloud is slightly larger and travels a little farther. Once again the first column shows the ramp up of the pressure, and the other columns show the growth and collapse of the cavitation cloud. The erratic pressure spikes at times: 0.0502, 0.0509, ... , 0.1174, 0.1181, 0.1187, 0.1196, 0.1197, 0.1204, are baffling. A plot of the pressure for the full discharge, Figure 3.5, shows the pressure for the entire cavitation event, and highlights these spikes in pressure. It is assumed that these spikes are due to gas bubbles trapped next to the transducer diaphragm that compressed and expanded during the discharge of the jet. The experimental setup allowed for excess gas to be released from the system to prevent compressibility from affecting the dynamic transducer. Multiple additional runs were taken after ensuring all gas was released from the system, but some of these runs occasionally resulted in pressure spikes similar to Figure 3.5. Without being able to visually determine whether or not there was any trapped gas it is difficult to definitively make any conclusions about the obvious pressure spikes.

The pressure spikes are again seen in Figure 3.6; a discharge from the 1.0 mm nozzle at 27.6 MPa (Re = 114,000). The first twelve frames of the third column show the formation of the cavitation cloud pulse. Around 0.0993 s the pressure spikes appear to affect the uniformity of the pulsation, as the cloud does not appear to form in the same way.

Comparisons to Figure 3.1 between jet diameter are shown in Figures 3.7 and 3.8. The small 0.7 mm diameter nozzle results in less intense cavitation, and the cloud is shorter and narrower (Fig. 3.7). The larger diameter 2.0 mm jet exhibited intense cavitation that propagated far downstream (Fig. 3.8). In order to fit the image sequence on the page, columns 1 and 2 are cropped to allow column 3 to show how much farther downstream the cloud propagated. The cloud collapsed outside of the frame. Measurements of the propagation lengths given in Section 3.1.2 required that the frame had a wider field of view to capture the entire jet.

The image sequences of Figure 3.9 and Figure 3.10 are representative comparisons between nozzle diameter and reservoir pressure. Figure 3.9 shows the cavitating jet from the 1.0 mm nozzle

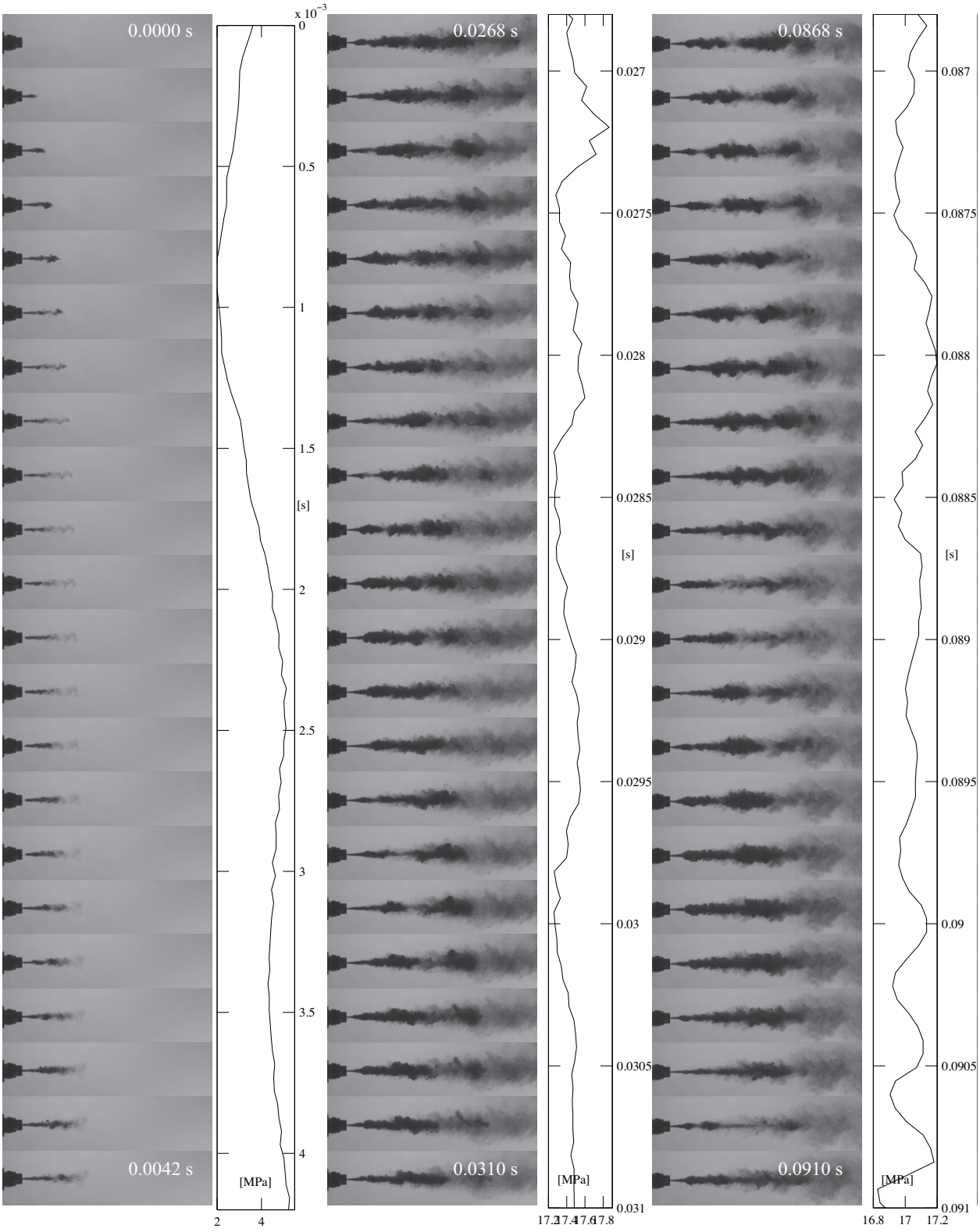

Figure 3.3: Image sequence with a Δt=0.0002 s of three time periods of a cavitating water jet from a 0.45 m long pipe with a 1.0 mm nozzle at 17.2 MPa (Re = 90,000). Time stamps show the time from cavitation inception. The cavitation is formed at the nozzle, moves downstream as a cloud, and collapses. The nozzle exit pressure as a function of time plotted to the right of each sequence shows jet pulsation (Frame rate: 5000; shutter: 1/10000 s; resolution: 768×128).

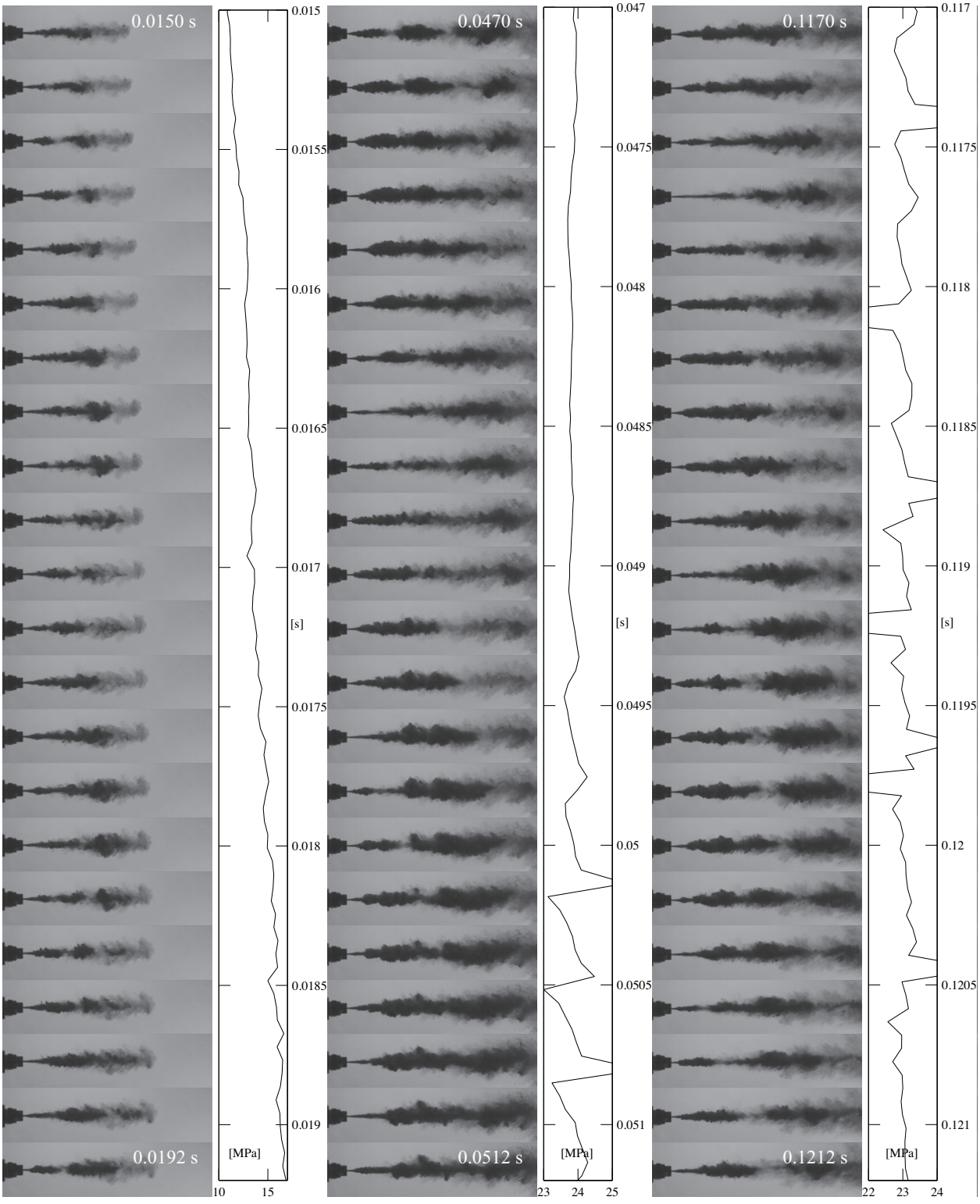

Figure 3.4: Image sequence with a Δt=0.0002 s of three time periods of a cavitating water jet from a 0.45 m long pipe with a 1.0 mm nozzle at 24.1 MPa (Re = 107,000). Time stamps show the time from cavitation inception. The cavitation is formed at the nozzle, moves downstream as a cloud, and collapses. The nozzle exit pressure as a function of time plotted to the right of each sequence shows jet pulsation (Frame rate: 5000; shutter: 1/10000 s; resolution: 768×128).

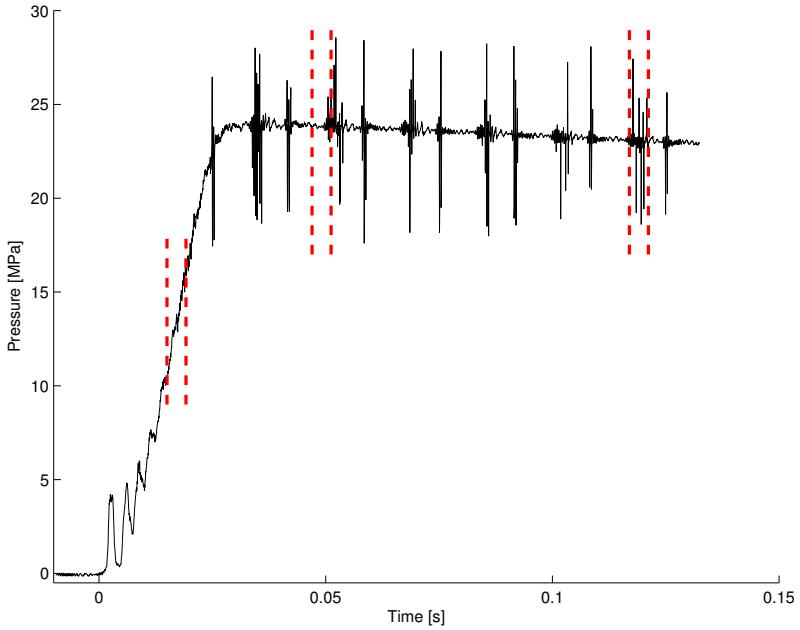

Figure 3.5: Pressure versus time plot for Figure 3.4. The leftmost pair of dashed lines is for the first column of Figure 3.1. The center pair of lines is for the center column of Figure 3.1. The rightmost pair of lines if for the third column of Figure 3.1 near the end of the life of the jet.

at the four test pressures (17.2 MPa, 20.7 MPa, 24.1 MPa, 27.6 MPa) with Re = 90,000–114,000 at approximately the same time (0.1000 s) after cavitation inception. This time, 0.1000 s, was chosen to avoid effects from the pressure ramp up and effects near the end of the jet discharge. Each of the sequences, (a)–(d), displays a cloud pulse and its propagation distance. The maximum propagation distance is manifested as the location beyond which the dark cavitation cloud fails to pass. It is here that the main collection of bubbles collapses. In all of the image sequences there are still what appear to be tiny bubbles traveling downstream after the general collapse of the cloud. This is the lighter gray shading in the images which lengthens and spreads over time. These seem to be remnant cavitation bubbles, but are extremely small and dispersed. It is unlikely that the lighter gray shading is a collection of gas bubbles from the pressurized gas or water supply, as this was not seen when the water jet was discharged at pressures less than one MPa. These smaller bubbles (gray areas) are not considered in any of the forthcoming measurements. The maximum distance the clouds propagate is shorter for the lowest pressure in sequence (a), and appears to increase with increasing pressure to sequence (d) where the maximum distance is the farthest.

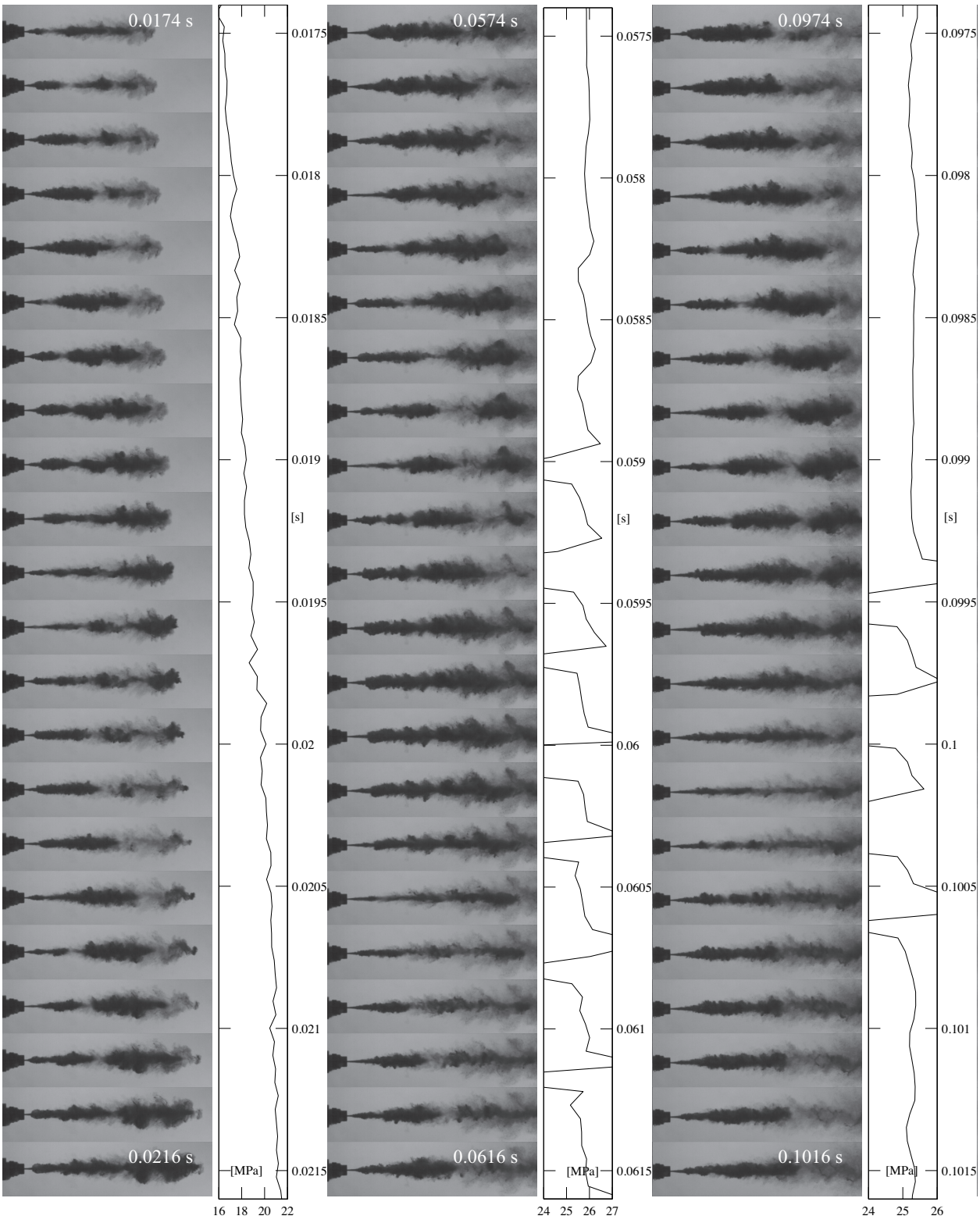

Figure 3.6: Image sequence with a Δt=0.0002 s of three time periods of a cavitating water jet from a 0.45 m long pipe with a 1.0 mm nozzle at 27.6 MPa (Re = 114,000). Time stamps show the time from cavitation inception. The cavitation is formed at the nozzle, moves downstream as a cloud, and collapses. The nozzle exit pressure as a function of time plotted to the right of each sequence shows jet pulsation (Frame rate: 5000; shutter: 1/10000 s; resolution: 768×128).

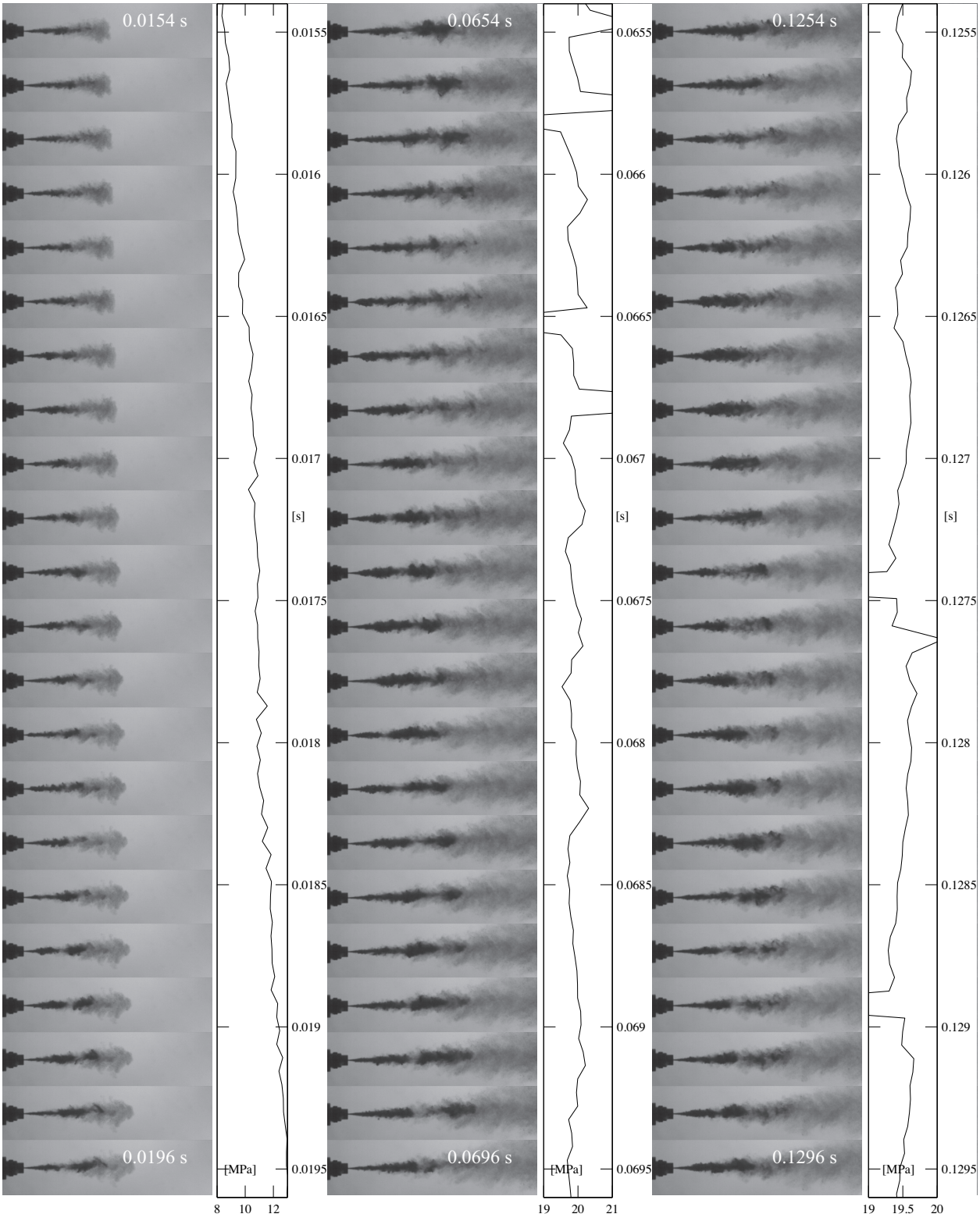

Figure 3.7: Image sequence with a Δt=0.0002 s of three time periods of a cavitating water jet from a 0.45 m long pipe with a 0.7 mm nozzle at 20.7 MPa (Re = 70,000). Time stamps show the time from cavitation inception. The cavitation is formed at the nozzle, moves downstream as a cloud, and collapses. The nozzle exit pressure as a function of time plotted to the right of each sequence shows jet pulsation (Frame rate: 5000; shutter: 1/10000 s; resolution: 768×128).

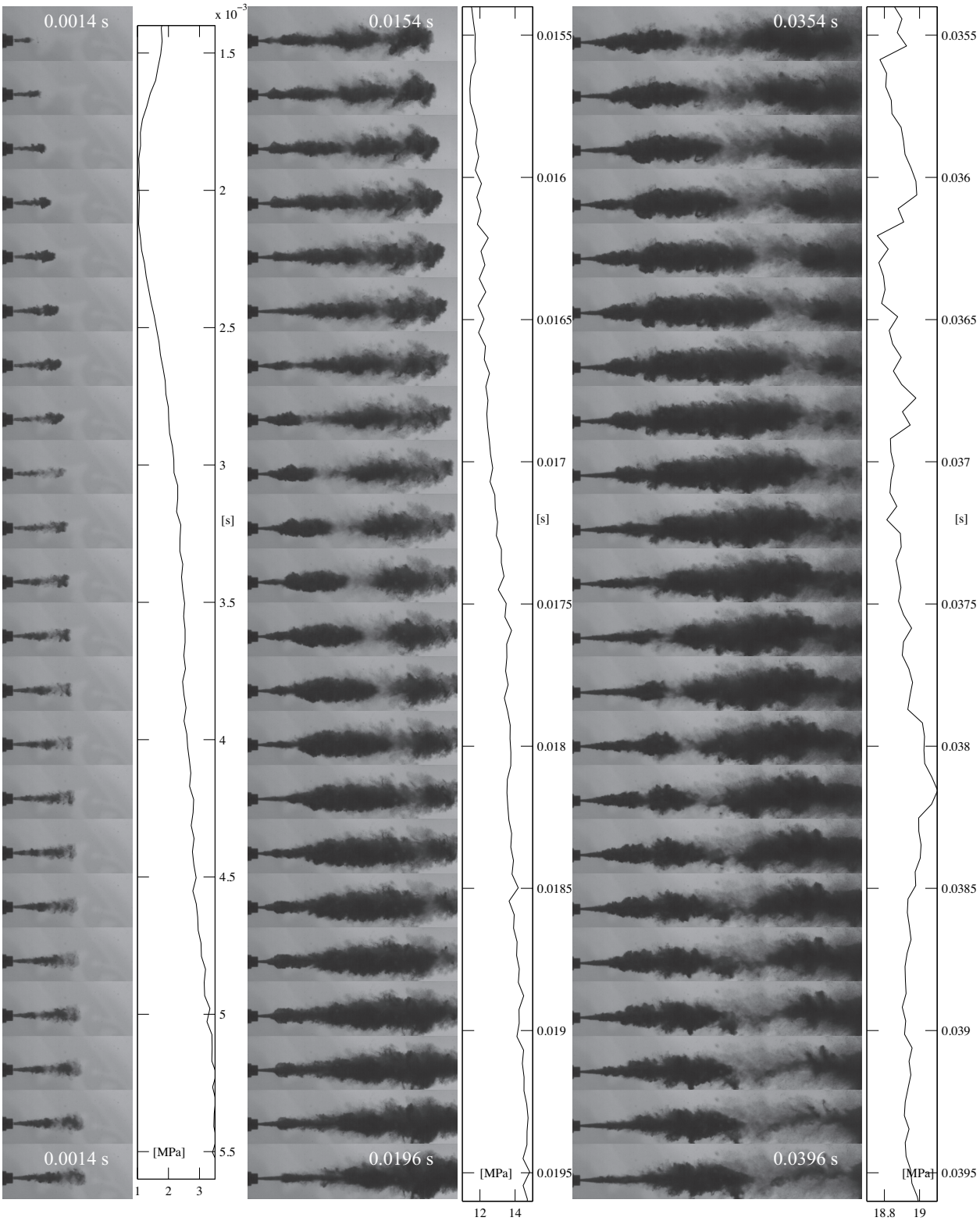

Figure 3.8: Image sequence with a Δt=0.0002 s of three time periods of a cavitating water jet from a 0.45 m long pipe with a 2.0 mm nozzle at 20.7 MPa (Re = 198,000). Time stamps show the time from cavitation inception. The cavitation is formed at the nozzle, moves downstream as a cloud, and collapses. The nozzle exit pressure as a function of time plotted to the right of each sequence shows jet pulsation (Frame rate: 5000; shutter: 1/10000 s; resolution: 768×128).

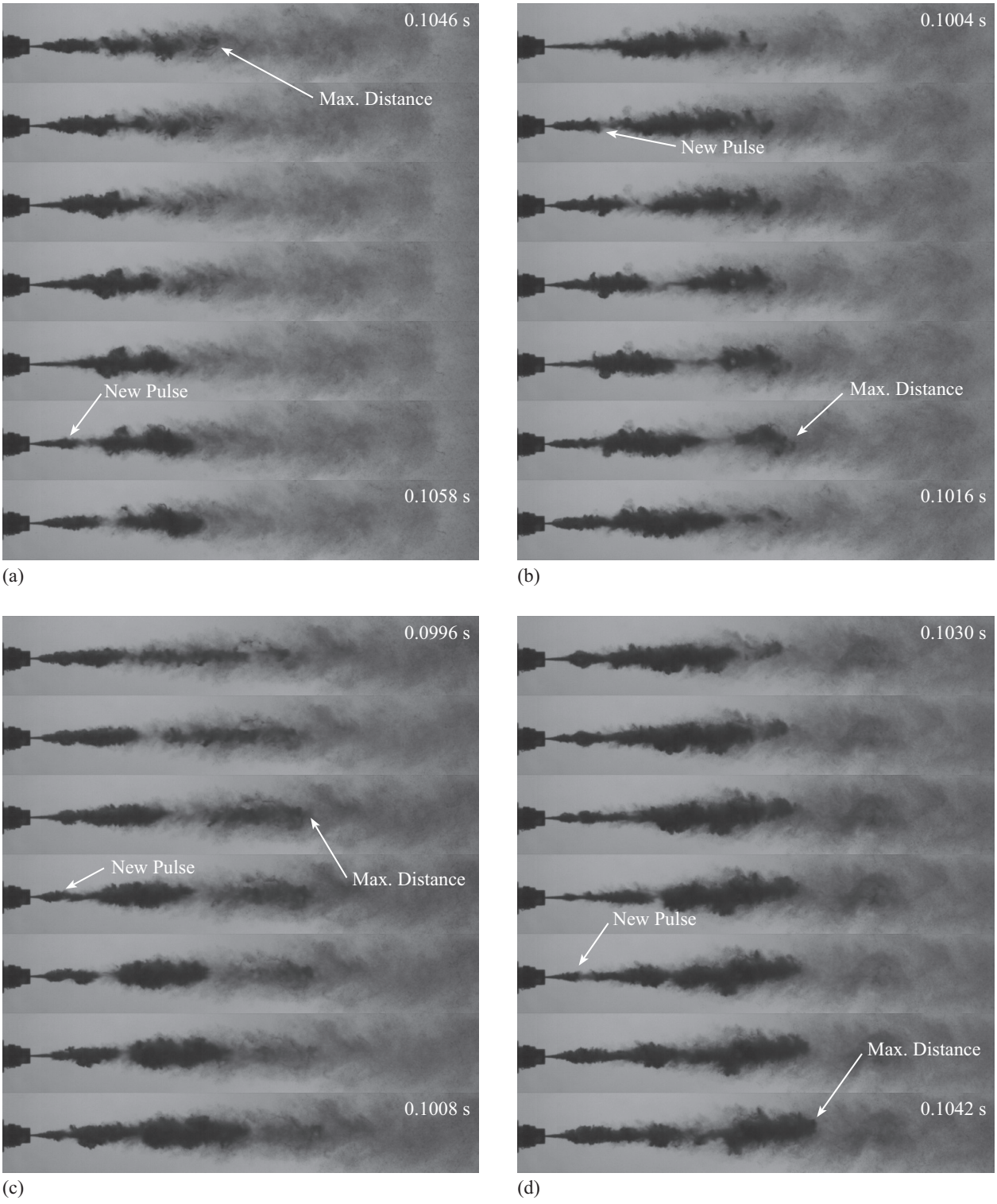

Figure 3.9: Comparison of cavitation (Δt=0.0002 s) from a 1.0 mm nozzle, 0.45-meter pipe at four pressures: (a) 17.2 MPa (Re = 90,000), (b) 20.7 MPa (Re = 99,000), (c) 24.1 MPa (Re = 107,000), (d) 27.6 MPa (Re = 114,000). Each sequence shows at least one new pulse and the maximum distance at which the cavitation cloud collapses. The pulsation and propagation distance are clearly marked for each pressure.

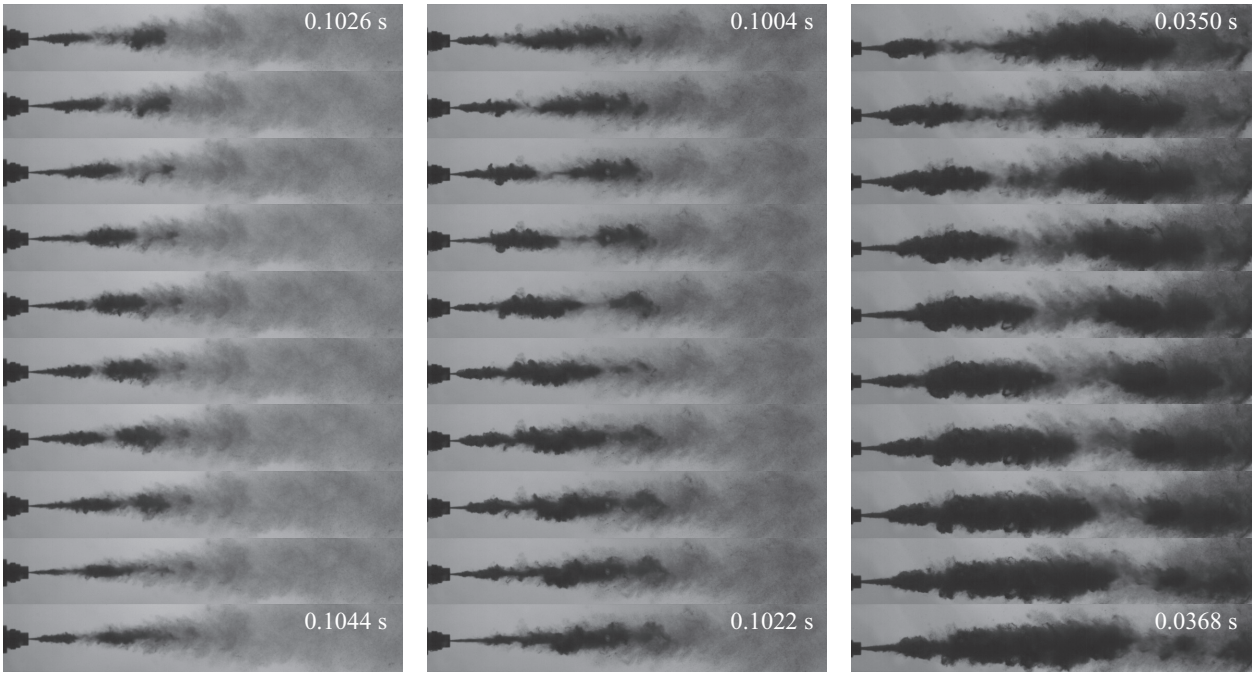

Figure 3.10: Cavitation cloud propagation is dependent on nozzle orifice diameter from the 0.45-meter pipe at 20.7 MPa for (a) 0.7 mm (Re = 70,000), (b) 1.0 mm (Re = 99,000), (c) 2.0 mm (Re = 198,000) diameter nozzle (Δt=0.0002 s). The cavitation cloud is much bigger as the nozzle diameter increases. Note that the cavitation cloud from the 2.0 mm diameter nozzle has a faster development and shorter total duration. It lasted less than 0.1000 seconds, so (c) shows 0.0350 s to 0.0368 s.

The relationship between cavitation cloud behavior for the three nozzles (0.7 mm, 1.0 mm, 2.0 mm) at 20.7 MPa is portrayed in Figure 3.10. Again the sequences begin around 0.1000 s, except sequence (c). The duration of cavitation from the 2.0 mm diameter nozzle was less than 0.1000 s. For this reason the 2.0 mm sequence, (c), begins at 0.0350 s instead. Each of the sequences portrays the jet in its fully-developed state; meaning that the pressure is at its steady value after ramping up from zero, as seen in Figures 3.2 and 3.5. The intensity of the cavitation is discernible as a darker cloud. There is a distinct separation between cavitation pulses evidenced by the lighter areas in the images, especially in (c). It is clear from these image sequences that larger exit orifices lead to more cavitation bubbles and farther propagation distances. Over the same length of time (0.0018 s) the 2.0 mm jet produced much more cavitation than the smaller 0.7 and 1.0 mm nozzles. All of these values are quantified in subsequent sections.

3.1.1 Duration of Cavitation

The length of time required for the column of water to be expelled through the nozzle depended on three variables: reservoir pressure, nozzle diameter, and pipe length. Without additional measurement techniques, the only way to measure the duration of the experiments was visually. This section presents measurements of the duration of each cavitation event, timed from the first visible cavitation bubbles until the nitrogen gas exited the nozzle.

Figure 3.11 shows the duration of the cavitation cloud as a function of the Reynolds number ($Re = Vd/\nu$). The data in this figure, and all subsequent plots, are differentiated by the test parameters. The length of pipe from which the jet discharged is shown by marker shape; triangle, square, and circle for the 0.45, 0.61, and 0.91 m pipes, respectively. Nozzle diameter is shown by

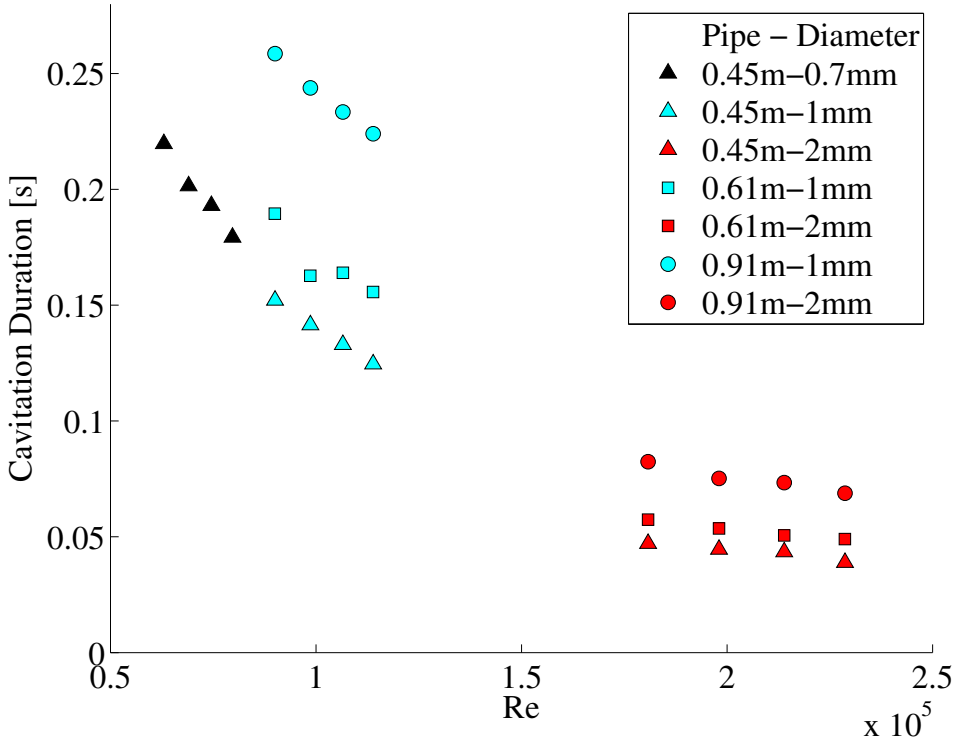

Figure 3.11: Time to discharge a column of water as a function of Reynolds number. Notice that higher Re resulted in shorter times. The larger 2.0 mm diameter nozzle discharged in a shorter amount of time than the smaller 1.0 mm diameter nozzle. Also, the discharge was faster for the shorter pipes, entirely based on volume flow rate.

marker color; black, blue, and red for the 0.7, 1.0, 2.0 mm diameter nozzles, respectively. The four test pressures are manifested by the conglomeration of the data in groups of four.

As expected from mass conservation; the duration of each discharge decreased as Re increased; the larger column of water took longer to be fully expelled from the nozzle. For example, visible cavitation issuing from the 0.91 m pipe with the 1.0 mm nozzle at 20.7 MPa (Re = 99,000) lasted 0.2438 s, but only lasted 0.1415 s from the 0.45 m pipe with the same nozzle and pressure (Re = 99,000). The columns of water also discharged faster through the larger 2.0 mm diameter nozzle than the smaller 1.0 mm nozzle. The discharge time from the 0.45 m pipe at 20.7 MPa was 0.1415 s from the 1.0 mm nozzle (Re = 99,000), and 0.0446 s for the 2.0 mm nozzle (Re = 198,000). Finally, it appears that higher pressure slightly decreased the discharge time. The duration of visible cavitation shortened by only 0.0275 s from 0.1521 s to 0.1246 s when the pressure was increased from 17.2 MPa to 27.6 MPa from the 1.0 mm nozzle and 0.45 m pipe (Re = 90,000 and 114,000, respectively).

3.1.2 Propagation Distance

Multiple measurements of the propagation distance were taken for each experimental run (see Table 2.1). For the primary pipe length, 0.45 m, a total of nine length measurements were made for each pair of parameters—nozzle diameter and jet pressure. There were a total of eight measurements taken for each run for the 0.61 m pipe, and only four measurements for each run for the 0.91 m pipe. Although fewer experiments were run for the longer pipes, pipe length did not seem to have a significant effect on the measurements, so more data were unnecessary.

The predicted propagation distances at the four test pressures, according to Equation 1.8, ranged from 0.3 m to 1.5 m downstream from the nozzle. The actual propagation distance was measured manually, as described in Section 2.4. Figure 3.12 visually shows that for a jet from the 0.45 m pipe at 20.7 MPa the nozzle diameter was the primary differentiator between the propagation distances. Measurements from the three images show that the cavitation cloud collapsed farther downstream at 27.8 cm for the 2.0 mm diameter nozzle (Re = 114,000) than the 0.7 mm diameter nozzle (Re = 70,000), which collapsed at only 11.7 cm, and the 1.0 mm diameter nozzle (Re = 99,000), which collapsed at 15.4 cm. In fact, this trend was the same for all experimental param-

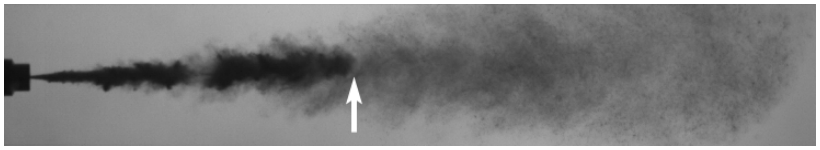

(a) 0.7 mm diameter nozzle; 11.7 cm

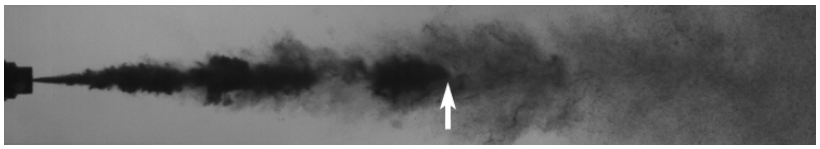

(b) 1.0 mm diameter nozzle; 15.4 cm

(c) 2.0 mm diameter nozzle; 27.8 cm

Figure 3.12: Maximum propagation distance marked by the arrow for each nozzle diameter, (a) 0.7 mm (Re = 70,000), (b) 1.0 mm (Re = 99,000), (c) 2.0 mm (Re = 198,000), from the 0.45-meter pipe at 20.7 MPa.

eter configurations. It is assumed that this occurred mainly because of the increased momentum of the column of water from the larger diameter nozzle.

The measured distances are much shorter than predicted. The theory predicts the length of a cavity behind a disk cavitator in a constant velocity flow. However, in the water jet experiments the velocity decreases significantly as the flow moves downstream. Energy is lost, thus the actual cavity cannot grow as large as the predicted cavity. The lost energy is likely due to viscosity, which was neglected in the equations resulting in the significant discrepancy.

Figure 3.13 illustrates the linear dependence of the propagation distance on the Reynolds number. The average collapse distance from the nozzle of the multiple measurements for each run is the value plotted in Figure 3.13. Scatter in the multiple data points and the method of calculating the lengths are accounted for in the uncertainty measurements as random and systematic uncertainty, respectively (see uncertainty in Appendix A.1 and MATLAB® scripts in Appendix A.2).

Nozzle diameter had the greatest effect on the cavitation cloud propagation distance, distinguished by color in the plots. The propagation distance for the smallest diameter nozzle (0.7 mm) was the shortest, ranging from 10 ± 1.45 cm to 13 ± 1.6 cm. The 1.0 mm nozzle resulted in

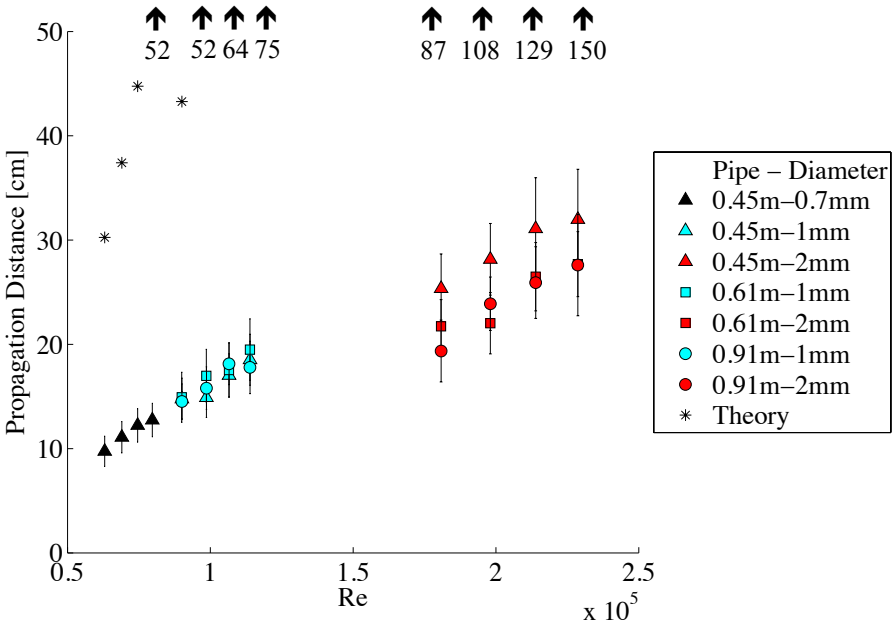

Figure 3.13: Comparison of propagation distance versus Reynolds number. Nozzle diameter has the greatest effect on cavitation cloud propagation distance. The distance increases with higher Re, but notice that the length of the water column had relatively no effect on the propagation distance. Theoretical distances are plotted for the given Re.

typical propagation lengths of 15±2.4 cm to 20±2.95 cm. The jet from the largest diameter nozzle (2.0 mm) had a wider range of possible distances traveled at 20±2.96 cm to 32±4.81 cm. Figure 3.13 shows that the pipe length, distinguished by marker shape, had seemingly no effect on the propagation distance, except for the 0.45 m pipe and 2.0 mm diameter nozzle. Pressure affected the distance somewhat, but in some cases this effect was less significant; compare the maximum propagation distances in Figure 3.9 where the four jets appear to all collapse in a similar location.

Based on this data, it can be concluded that for the tested parameters larger diameter jets are capable of longer distances. This trend is significant in that it outlines how the jet parameters can be scaled. A change in the diameter of the jet affects both Re and the propagation distance. Future work calls for a larger-scale experiment, and the relationship between propagation distance and Reynolds number will be essential to scaling up the jet. Future work is described further in Section 4.2.

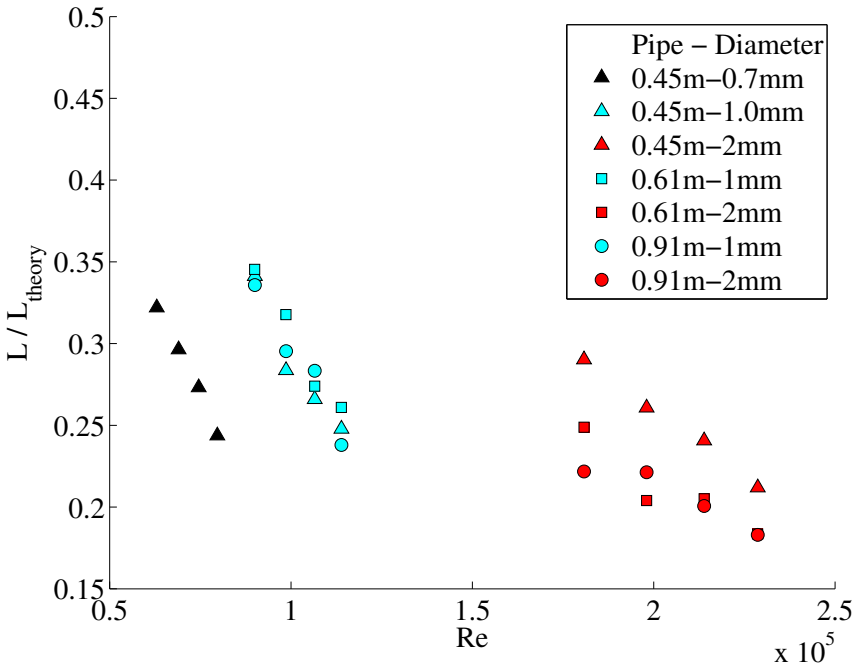

Figure 3.14: Non-dimensionalized propagation distance versus Reynolds number. Clear separation along the horizontal axis is an effect of the jet diameter. Vertical scatter is from the different lengths of pipe.

Figure 3.14 compares the non-dimensional propagation distance to Reynolds number. The length was non-dimensionalized by the predicted length of the cavity from Section 1.3. The data are grouped in sets of four by the test pressure, and in color by the nozzle diameter. This plot illustrates the large discrepancy between the theoretical and measured propagation distances. The discrepancy increases with jet pressure.

3.1.3 Cavitation Cloud Width

One of the measured traits of the cavitation clouds was the typical width of the cloud. Once cavitation began the cloud expanded radially, as well as longitudinally to a certain size before fully collapsing. After collapsing, smaller bubbles continued to spread, but the exact makeup of these is uncertain and their expansion was neglected. Only the width of the main cloud was measured. The previous image sequences illustrate how the main cavitation cloud had limited width expansion. This characteristic allowed for measurements of the typical cloud width to be made.

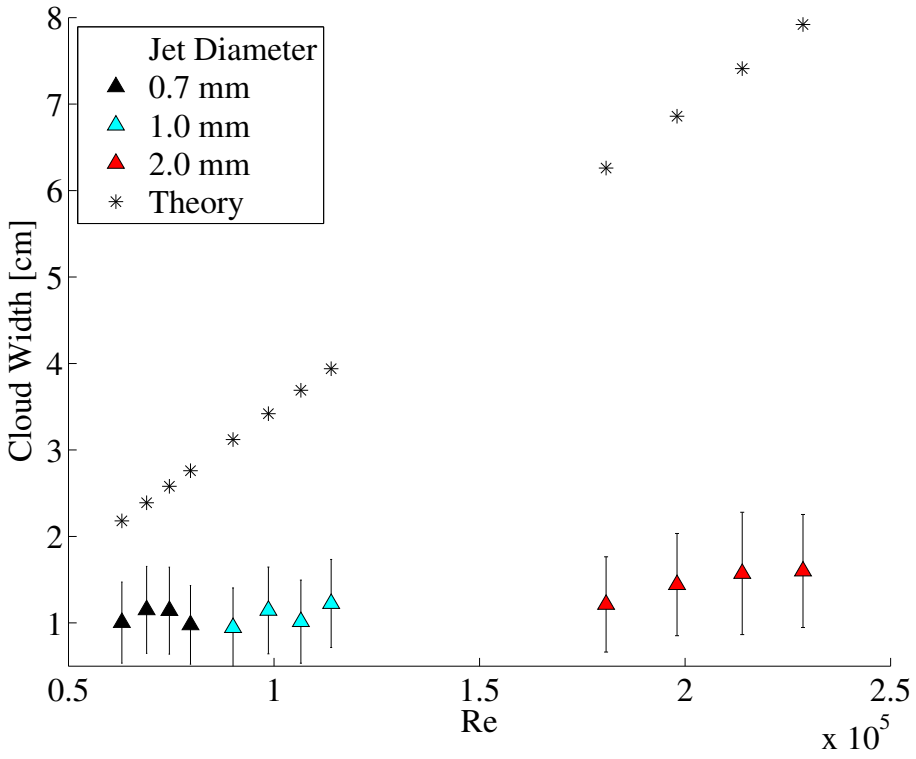

Figure 3.15: Cavitation cloud width versus Reynolds number. The 2.0 mm jet exhibited wider cavitation clouds than the 1.0 mm or 0.7 mm jet, but all measured values became increasingly different from predicted widths. The pulsatory nature of the jets dramatically influences the experimental uncertainty.

Multiple width measurements were taken for each run of the three nozzles and four pressures. The measurements were taken at a point downstream where the main cavitation cloud reached its maximum width, which was not dependent on the length of pipe used. This point was closer to the nozzle for the shorter propagating clouds, and farther from the nozzle for the longer propagating clouds.

Figure 3.15 shows the average cloud width for cavitation for each of the nozzle diameters and pressures tested. The predicted widths from Equation 1.7 were between 2.2 cm for cavitation from the 0.7 mm nozzle at the lowest pressure and 7.9 cm for cavitation from the 2.0 mm nozzle at the highest pressure. The discrepancy between the measured and predicted widths in Figure 3.15 increases with Re. The same reasoning as that used for the propagation length discrepancies is again used here–viscosity and constant flow velocity were not considered in the predictions. The measured widths for all three nozzle diameters are close together, ranging from 0.95 cm to 1.6

cm. As can be seen in the figure, significant measurement uncertainty exists; which is primarily due to the rapid diameter changes as the cavity pulsated. The width visibly increased with nozzle diameter, but these experiments emphasize that the cloud width is not as dependent on jet velocity as the theory predicts.

3.1.4 Cavitation Cloud Area

In addition to the length and width measurements of the cavitation cloud, the longitudinal cross-sectional area was also measured, as described in Section 2.4. It should be noted that this area is not simply the product of the length and the width of the cloud, but is measured by counting the number of pixels. Figure 3.16 illustrates the dependence of the cloud area on the Reynolds number. The relationship is distinctly linear. The linear relationship between cloud area and Re is similar to that illustrated in Figure 3.13, meaning the area is more dependent on the propagation

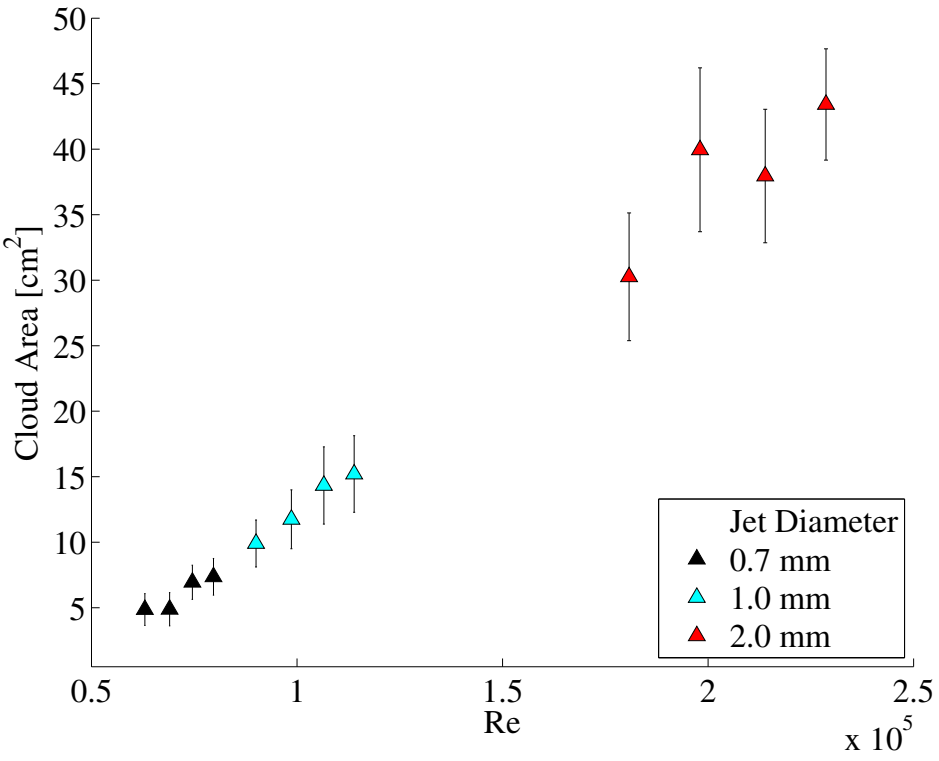

Figure 3.16: Comparison of the cavitation cloud area versus Reynolds number. The 2.0 mm jet generates a larger cavitation cloud than the smaller diameter jets.

length than the cloud width. The nozzle diameter, specifically, had a major impact on the size of the cavitation cloud. The points plotted in Figure 3.16 show the average area over the life of the cavitation for each experimental run. Data for the three pipe lengths are combined into a single point for each Reynolds number.

Over the range of test pressures the cloud from the 2.0 mm nozzle covered a larger area (30 and 45 cm^2) than the cloud from the 1.0 mm (10-17 cm^2) and 0.7 mm nozzles (5-9 cm^2). These results are distinctly visible in the image sequence of Figure 3.10, which compares cavitation between the three nozzle diameters.

3.1.5 Pulsation Frequency

As can be seen in the sequences of Figures 3.1, 3.3, 3.4, 3.6–3.10 the jet exhibited an interesting pulsation as the water was forced through the nozzle. Previous researchers have described this pulsation and some associated trends, but failed to quantify the frequencies of these pulsations (see [13–16]). The high-speed camera, as well as the dynamic pressure transducer, recorded this pulsation. A trend for the pulsation rate was determined from the images according to the variation of image intensity for a single column of pixels, by the method previously described in Section 2.4.

In Figure 3.17 the most prominent two or three frequencies of the pulsing cavitation cloud for each run are plotted versus the Reynolds number. All of the frequency data are plotted to illustrate trends in the data. These trends would not be noticeable if only a single average frequency had been plotted for each experimental run. The plotted frequencies are noticeably clustered according to nozzle diameter. The longer pipes were included in the study initially under the suspicion that pipe length would greatly influence the pulsation frequency. This proved to not be the case, as manifested in the frequency plot.

Just as with the propagation distance the pulsation frequency of each jet depended more on nozzle diameter than reservoir pressure or pipe length. The cavitation from each diameter jet appears to be grouped by frequency as well. There appears to be a slight decrease in frequency with increasing Reynolds number, which matches the trend described by Hutli [15], where the frequency decreased as the jet pressure increased. Jets from the largest diameter nozzle (2.0 mm) exhibited generally lower frequency content ranging from 250 Hz to 600 Hz. Jets from the 1.0 mm nozzle had pulsations ranging between 450 Hz and 800 Hz. The smallest diameter jets (0.7

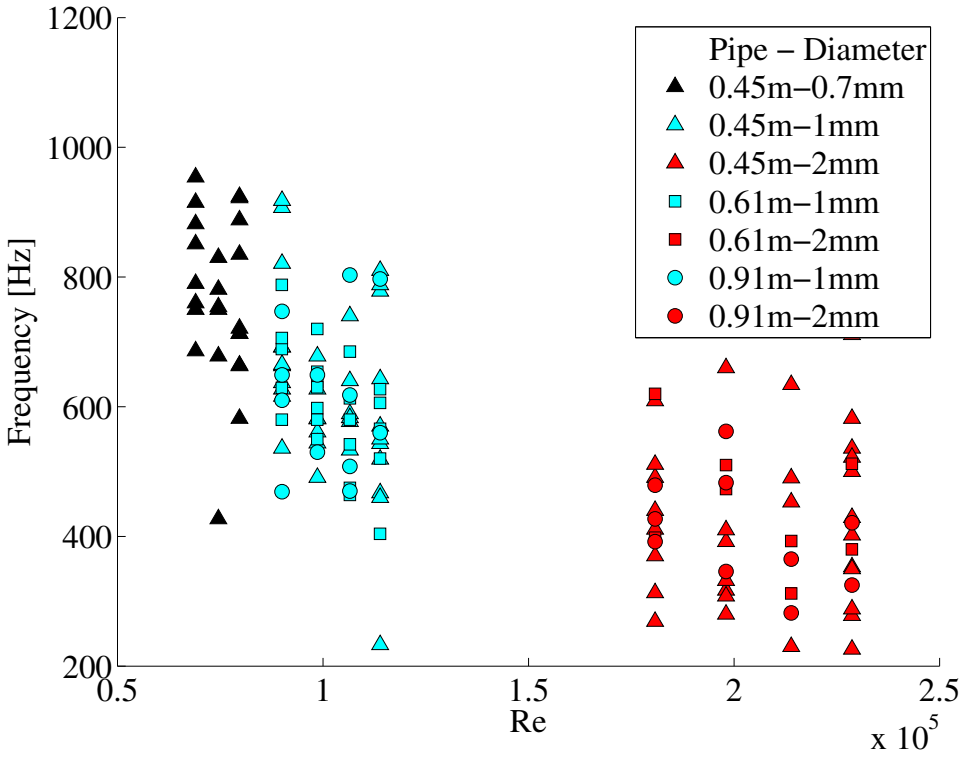

Figure 3.17: Cavitation cloud pulsation frequencies versus Reynolds number. The pulsation frequency was dependent on nozzle diameter, as seen by the color groupings, and jet pressure. The primary pulsation frequency of the cavitating jet for the 2.0 mm diameter nozzle ranged between 250–600 Hz. The range for the jet with the 1.0 mm diameter nozzle was 450–800 Hz. The 0.7 mm diameter nozzle gave the jet a pulsation frequency greater than 700 Hz.

mm) pulsed at higher frequencies between 700 Hz and 1000 Hz, generally. Frequency analysis of the images and pressure data included signals around 100–130 Hz, which are not included in Figure 3.17. Analysis of a group of images without cavitation resulted in only frequencies in this range, and it was determined to be caused by the flickering of the backlighting. The pressure data exhibited frequencies similar to those of the images, even the 100–130 Hz oscillations. It is assumed that this is because the computer was plugged into the AC wall power.

3.1.6 Cloud Front Velocity

Each cavitation cloud grew longitudinally and spread radially as it moved away from the nozzle. This action resulted in decreased velocity and energy downstream. It was expected that higher reservoir pressures resulted in faster downstream velocities. Theoretically, for the experi-

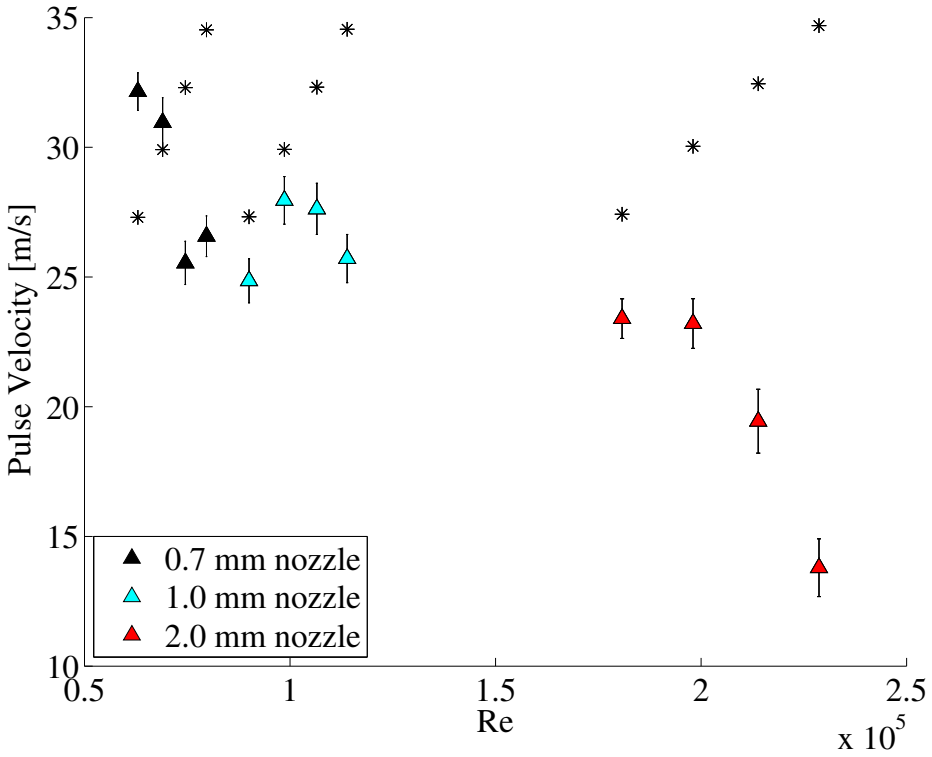

Figure 3.18: Front velocity of cloud pulses versus Reynolds number. The measured values are closer to the predicted velocities for the 0.7 mm diameter nozzle than the measured velocities for the 1.0 mm and 2.0 mm diameter nozzles. The same relationship to jet pressure shown by the theoretical front velocity is not seen in the measured data.

mental parameters in this study the exit velocity of the jet ranged from 100 m/s to 127 m/s. These values were pressure-dependent and nozzle diameter-independent. The velocity of the front of the cavitation cloud just before it collapsed was measured and compared to the predicted front velocity from Section 1.3. This measurement was sensitive to the location at which it was taken. The cloud front velocity decreased dramatically from the nozzle exit to the point of collapse because of mainly viscous effects.

Figure 3.18 shows the relationship between cloud front velocity and the Reynolds number of the jet. The plotted data are the average front velocity of multiple sets of images for each run. Pipe length had minimal effect on the front velocity, so all of the data from the three pipes are averaged into the single value plotted for each set of parameters. Error bars are included to show that the measurement uncertainty was typically only $\pm$1–2 m/s. The nozzle diameter has little effect on the predicted front velocity. From Equation 1.5 the front velocity is dependent

on the jet exit velocity, which at each test pressure was constant for the three nozzle diameters. The predicted velocities increased with pressure for each nozzle diameter, as seen in Figure 3.18. The experimental data do not follow the trend of increased front velocity for increased pressure. There is a weak correlation of the opposite trend where the experimental front velocity decreases with increasing Re. This decrease in front velocity from low Re to higher Re is common for the measurements of all three nozzle sizes.

The sensitivity of the measured velocity on the location downstream could be the reason that the data do not follow the predicted trends. As previously stated, the predicted values from Equation 1.5 are based on the initial jet velocity and the area drag due to the diameter of the cavity. The distance downstream at which the velocity measurement is made is not taken into account in these predictions. Additionally, the initial jet velocity is independent of the nozzle diameter, but the propagation distance is not. Once the cavitation bubbles are formed the higher Re jets (larger nozzle diameter and higher pressures) result in farther propagation distances; assumedly because the larger diameter jets have greater momentum, and higher pressure gives higher initial velocity. The longer distance traveled results in more energy being lost to effects like viscosity. The lower energy then causes the front velocity to be reduced, as was measured. Preliminary measurements of the front velocity at relatively the same location downstream from the nozzle for each run showed that the velocity would more likely follow a trend of increasing with Re.

3.1.7 Cavitation Erosion

An attempt was made to erode solid material with this experimental water jet. Due to the setup of the jet this proved difficult. Cavitation is known to erode even the strongest materials. To test whether this jet would erode solid material placed downstream from the nozzle multiple discharges were fired at a piece of clear polystyrene. The solid polystyrene was placed 22 cm away from the nozzle, a few centimeters short of the maximum average propagation distance for the nozzle and pressure used. The nozzle diameter was 2.0 mm and the pressure used was 20.7 MPa, giving a Re = 198,000. It was assumed that even a few small eroded pits would be visible in the clear solid since tiny scratches are visible. The jet was aligned with the solid specimen and discharged 30 times at the clear polystyrene. Each discharge was monitored visually to ensure that it hit the solid surface. When the solid was removed from the water, there were no visible

markings. No further testing was completed due to the length of time necessary and inconvenience of running each test. In the literature it can take hundreds of jet pulses to affect any measurable erosion. Future work is needed to adapt this mechanism to be able to be easily discharged many times to erode a solid downstream.

3.2 Conclusion

This chapter presented the experimental results from a cavitating submerged water jet. The behavior of the cavitation cloud was outlined with respect to the experimental parameters: nozzle diameter, jet pressure, and water column length. Image sequences showed how the cavitation cloud developed and propagated downstream. Longer pipe lengths lengthened the time it took to discharge the jet, but affected little else. The jet lasted approximately 0.22 s longer when the pipe length was doubled from 0.45 m to 0.91 m. The propagation length was shown to be highly dependent on the nozzle diameter, and less so on the jet velocity. The measured lengths were shorter than what was predicted, only ranging between 10–35 cm. Other geometric factors, such as width and longitudinal area, were also measured, and show that increasing the jet diameter resulted in greater cavitation. Each experimental case exhibited an interesting pulsation that was quantified according to Reynolds number. The ultimate differentiator turned out to be the jet diameter. Cavitation from jets with larger diameters pulsed at slightly lower frequencies, generally. The frequency ranges for the three nozzle diameters, 0.7 mm, 1.0 mm, 2.0 mm, were $>$700 Hz, 450–800 Hz, and 250–600 Hz, respectively. Finally, the velocity of the front of the cavitation cloud was measured and described in spite of some measurement challenges. An attempt was made to erode a solid material with the cavitation cloud. The inconvenience of the experimental setup prevented any measurable damage from being done. This is where significant future work is necessary.

CHAPTER 4. CONCLUSIONS

The research presented in this thesis described the behavior of cavitation clouds from a submerged water jet. Before cavitation clouds could be studied, a means of generating cavitation had to be developed. A column of water discharged by ultrahigh-pressure nitrogen through a small-diameter nozzle was the method used. There are various ways of generating cavitation and this method was suited to the investigation of the behavior of cavitation clouds.

4.1 Summary

An axisymmetric water jet will cavitate when submerged in water if its velocity is sufficiently high. For a column of water discharged into quiescent water by pressurized gas at pressures from 17.2 to 27.6 MPa this cavitation appeared as a cloud of small bubbles. The cavitation cloud exhibited a pulsation behavior that has not been fully quantified in the literature. Here it was shown that the frequency at which the cloud pulsed was dependent on Reynolds number of the water jet (see Figure 3.17). The frequency of pulsation decreased as the jet velocity and diameter increased. It was found that low Re jets resulted in higher frequencies. For Re $<$ 80,000 the range of common frequencies was 500–1000 Hz. For higher Re = 80,000–120,000, the range was approximately 400–800 Hz. The highest Re = 180,000–230,000, exhibited slightly lower frequencies, 250–600 Hz.

Each pulse of cavitation traveled away from the nozzle until it collapsed. The distance at which this collapse occurred was also shown to be linearly dependent on Re, but more specifically on the nozzle diameter. The distance increased as the diameter of the jet increased. For Re = 60,000–80,000 the distance traveled until collapse was approximately 10–14 cm. For Re = 90,000–120,000 the distance was 15–20 cm. For Re = 180,000–230,000 the distance was 17–32 cm.

The longitudinal area and average width were measured to show how the cavitation expanded from a thin water jet. Again, these were dependent on Re. The cloud area increased lin-

early with Re, whereas the width of the cloud followed a less distinct trend. The average maximum cloud width remained relatively constant, around 1.2 cm, for all cases tested.

Lastly, it was determined that the relationship between the experimental parameters and the velocity of the front of the cavitation cloud was somewhat less clear. The location at which the velocity measurements were made played a significant role in what the data showed. The front velocity decreases with Re, which was not what the theory predicted. As with some of the other measurements, the fact that viscosity was neglected greatly affected how the experimental and theoretical data were related.

4.2 Future Work

There have been myriad studies related to cavitation. This research focused on one particular aspect related to clouds of cavitation bubbles. The hope is that this work forms a foundation for future research using a cavitating water jet to erode solid materials at a distance in underwater environments.

At this time, a proposal has been written to a federal agency, the Strategic Environmental Research and Development Program, to use cavitation from a water jet as a way to disassemble unexploded ordnance (UXO) in submerged environments. Currently, there are no environmentally friendly ways to eliminate UXO underwater. A device to cut the material into pieces from which the explosives could be easily removed without contaminating the environment has been proposed.

In order for the research presented here to be of use for this device further research is necessary. A numerical model is being developed at the Naval Undersea Warfare Center to allow the adjustment of design parameters. This model needs to be validated and tested. With this model a scaled-up cavitating jet could be tested to determine the maximum propagation distance, and thus, the distance away from a solid at which the solid could be effectively cut. Once the model is used to determine what size of a jet is necessary, a full-scale jet would be built and tested in a submerged environment.

The previous research presented in Chapter 1 shows that cavitation erosion has the potential to be an effective cutting mechanism. If a cavitation device that can remotely cut submerged solids without polluting its surroundings is developed many underwater environments will become safer for commercial and private use.

REFERENCES

[1] Parsons, C. A., and Cook, S. S., 1919. "Investigations into the causes of corrosion or erosion of propellers." *Journal of the American Society of Naval Engineers,* **31**(2), pp. 536–541. 1, 3

[2] Reynolds, O., 1901. "Experiments showing the boiling of water in an open tube at ordinary temperatures." *Papers on Mechanical and Physical Subjects,* **2**, pp. 578–587. 2

[3] Kornfeld, M., and Suvorov, L., 1944. "On the destructive action of cavitation." *Journal of Applied Physics,* **15**, pp. 495–506. 3, 5

[4] Cook, S. S., 1928. "Erosion by water hammer." *Proceedings of the Royal Society of London,* **119**, pp. 481–488. 3, 4, 5, 6

[5] Knapp, R., Daily, J., and Hammitt, F., 1970. *Cavitation*. McGraw-Hill Book Company, New York. 4, 5

[6] Munson, B. R., Young, D. F., and Okiishi, T. H., 2006. *Fundamentals of Fluid Mechanics*., fifth ed. John Wiley and Sons, Inc. 4, 6

[7] Wu, X., and Chahine, G., 2007. "Characterization of the content of the cavity behind a high-speed supercavitating body." *Journal of Fluids Engineering,* **129**, pp. 136–145. 4

[8] Rayleigh, L., 1917. "On the pressure developed in a liquid during the collapse of a spherical cavity." *Philosophical Magazine,* **34**, pp. 94–98. 4, 6

[9] Ooi, K. K., 1985. "Scale effects on cavitation inception in submerged water jets: a new look." *Journal of Fluid Mechanics,* **151**, pp. 367–390. 4

[10] Gopalan, S., Katz, J., and Knio, O., 1999. "The flow structure in the near field of jets and its effect on cavitation inception." *Journal of Fluid Mechanics,* **398**, pp. 1–43. 4, 6

[11] O'Hern, T. J., 1990. "An experimental investigation of turbulent shear flow cavitation." *Journal of Fluid Mechanics,* **215**, pp. 365–391. 4, 6

[12] Soyama, H., Yanauchi, Y., Sato, K., Ikohagi, T., Oba, R., and Oshima, R., 1996. "High-speed observation of ultrahigh-speed submerged water jets." *Experimental Thermal and Fluid Science,* **12**, pp. 411–416. 4, 6

[13] Trilling, L., 1952. "The collapse and rebound of a gas bubble." *Journal of Applied Physics,* **23**(1), pp. 14–17. 24, 42

[14] Strasberg, M., 1953. "The pulsation frequency of nonspherical gas bubbles in liquids." *Journal of the Acoustical Society of America,* **25**(3), pp. 536–537. 24, 42

[15] Hutli, E., and Nedeljkovic, M., 2008. "Frequency in shedding/discharging cavitation clouds determined by visualization of a submerged cavitating jet." *Journal of Fluids Engineering,* **130**. 5, 42

[16] Sato, K., Sugimoto, Y., and Ohjimi, S., 2009. "Structure of periodic cavitation clouds in submerged impinging water-jet issued from horn-type nozzle." In *Ninth Pacific Rim International Conference on Water Jetting Technology*. 5, 42

[17] Sato, K., Sugimoto, Y., and Ohjimi, S., 2009. "Pressure-wave formation and collapses of cavitation clouds impinging on a solid wall in a submerged water jet." In *Seventh International Symposium on Cavitation CAV2009*. 5, 24

[18] Hansson, I., and Morch, K. A., 1980. "The dynamics of cavity clusters in ultrasonic (vibratory) cavitation erosion." *Journal of Applied Physics,* **51**(9), pp. 4651–4658. 5, 24

[19] Reisman, G. E., Wang, Y. C., and Brennen, C. E., 1998. "Observations of shock waves in cloud cavitation." *Journal of Fluid Mechanics,* **355**, pp. 255–283. 5

[20] Philipp, A., and Lauterborn, W., 1998. "Cavitation erosion by single laser-produced bubbles." *Journal of Fluid Mechanics,* **361**, pp. 75–116. 5, 6

[21] Coleman, S. L., and Scott, V. D., 1995. "Comparison of tunnel and jet methods for cavitation erosion testing." *Wear,* **184**, pp. 73–81. 5, 6

[22] Bourne, N. K., and Field, J. E., 1995. "A high-speed photographic study of cavitation damage." *Journal of Applied Physics,* **78**(7), p. 4423. 5

[23] Brujan, E. A., Keen, G. S., Vogel, A., and Blake, J. R., 2002. "The final stage of the collapse of a cavitation bubble close to a rigid boundary." *Physics of Fluids,* **14**(1), pp. 85–92. 5, 6

[24] Jayaprakash, A., Chahine, G., and Hsiao, C. T., 2010. "Numerical and experimental study of the interaction of a spark-generated bubble and a vertical wall." In *ASME 2010 International Mechanical Engineering Congress and Exposition*. 5, 6

[25] Lu, J., Xu, R. Q., Chen, X., Shen, Z. H., Ni, X. W., Zhang, S. Y., and Gao, C. M., 2004. "Mechanisms of laser drilling of metal plates underwater." *Journal of Applied Physics,* **95**(8), pp. 3890–3894. 6

[26] May, A., 1975. Water entry and cavity-running behavior of missiles 75-2 Tech. rep., NAVSEA Hydroballistics Advisory Committee, http://www.dtic.mil/cgi-bin/GetTRDoc?AD=ADA020429&Location=U2&doc=GetTRDoc.pdf. 7, 8

[27] Savchenko, Y. N., 2001. "Supercavitation–problems and perspectives." In *CAV 2001: Fourth International Symposium on Cavitation*. 7, 22

[28] Figliola, R., and Beasley, D., 2006. *Theory and Design for Mechanical Measurements*., fourth ed. John Wiley and Sons, Inc. 15, 51

APPENDIX A. UNCERTAINTY AND MATLAB® SCRIPTS

A.1 Uncertainty Calculations

This section shows the calculation steps to determine the experimental uncertainty of the various length measurements, and other measurements. The process is according to Figliola [28]. That text is where the student-t values were found as well. The equations are listed in this section, but the calculations of the values are done in the MATLAB® codes listed in Section A.2.

The static and dynamic pressure measurements had errors of ± 1.1 MPa and ± 0.5 MPa, respectively. These were acceptible, as pressure did not greatly affect any of the test results.

The random error resulting from multiple measurements is found from the equation:

$$P = \sqrt{\Sigma (P_i)^2} \tag{A.1}$$

$$P_i = \frac{S_i}{\sqrt{N_i}}, \tag{A.2}$$

where S_i is the standard deviation of the measured values, and N_i is the number of values. The systematic error from the measurement calculations is given by:

$$B = \sqrt{\left(\frac{\partial L}{\partial calibration} U_{calibration} \right)^2}. \tag{A.3}$$

The calibration factors are listed in 2.3. $U_{calibration}$ is the error in picking pixels set to 5 pixels. L is the equation of what is being measured; this is either length, velocity, area, etc. The total uncertainty is found from the following equation:

$$U_{Total} = \sqrt{B^2 + (t_{\alpha\nu} P)^2}, \tag{A.4}$$

where $t_{\alpha\nu}$ is the student-t value for the number of measurements. The probability I used was 95%.

A.2 MATLAB® Scripts

A.2.1 Propagation Distance

The propagation distance was measured with this code and each value was loaded into the next code:

```
% Cavitation Measurements
% Michael Wright
% October 28, 2011
 clc
clear all
% Create [NxMxj] 3D array where each image is [NxMx1]
% Create list of files into an array

fiLes = dir('/Volumes/WRIGHTDRIVE/Supercav_BYU/JET/...
Images/Images18/07mm/2500_1/*.tif');
newpath = '/Volumes/WRIGHTDRIVE/Supercav_BYU/JET/...
Images/Images18/07mm/2500_1/';
%--------------------------------------------------------------------------
addpath(newpath)
x = 2320;
y = x+100;
for j = x:20:y
    imshow(fiLes(j).name);
    iMage(:,:,j) = imread(fiLes(j).name);  % Read in each image to a 3D array
    imshow(iMage(:,:,j)) % Show image on the screen
    n = 1;      % Number of distances desired
    M(:,:,j) = ginput(2*n);        % [X,Y,image #] of chosen points
    % Count the number of pixels between chosen points
    % In piXels each row contains the measurements from a single image
    for i = 1:n
```

```
        piXels(j,i) = sqrt((M(2*i,1,j)-M(2*i-1,1,j))^2 +...
          (M(2*i,2,j)-M(2*i-1,2,j))^2);
        % Conversion factor for each run:  pixels/cm
          cFc = 25.02;
          cFf = 20.7;
          cF24 = 19.5;
          cF36 = 19.25;
    end
end
close all
piXels;
Length = piXels./cFf;    % Length of jet in cm
L = Length(Length~=0)
```

A.2.2 Length Uncertainty

The length measurements taken from the previous code are plotted here, and include the measurement uncertainty.

```
 clc;
clear all
% Length output from processing (Row is pressure)
L187 = [10.6 10.4 8.48 11.993 6.742 9.353 11.867 9.233 9.033;
        14.232 11.713 9.322 11.35 10.793 9.952 10.472 11.112 10.834;
        12.79 10.796 10.75 13.67 13.15 10.23 13.315 12.912 12.432
        12.842 12.232 13.11 13.631 12.632 11.592 12.994 14.39 11.232];

L181 = [15.072 14.029 14.988 14.75 16.747 12.151 12.31 17.549 15.348;
        17.626 13.71 15.428 14.11 14.588 15.788 14.19 15.188 13.43;
        17.506 17.715 17.467 16.187 17.747 16.428 17.388 15.629 17.146;
        15.108 18.466 20.744 21.103 17.786 19.824 19.864 17.186 16.667];
```

```
L182a =[28.382 28.738 25.38 27.578 26.542 24.145 22.91 21.903 22.539;
        27.818 27.099 28.937 29.618 29.658 28.898 26.14 26.661 28.577];

L182b =[25.845 30.486 32.611 35.508 35.413 34.058 30.097 26.042 29.76;
        31.161 34.832 34.252 32.609 30.93 31.014 27.006 34.941 31.014];

L241 = [17.231 14.052 15.846 14.564 15.847 13.847 16.564 11.436;
        17.385 15.949 19.181 16.923 17.128 16.615 15.897 16.821;
        17.951 18.104 17.646 17.181 18.616 17.283 18.308 15.181;
        16.667 20.821 19.744 19.898 19.949 20.564 20.667 17.693];

L242 = [20.872 21.18 21.026 23.847;
        21.181 19.541 24.308 23.078;
        23.488 27.18 28.053 27.231;
        28.821 28.615 25.694 27.643];

L361 = [13.507 15.065 14.234 15.325;
        14.597 15.065 17.663 15.896;
        19.169 18.39 17.664 17.351;
        18.702 16.364 20.052 16.052];

L362 = [16.832 22.082 17.87 20.68;
        23.273 23.898 24.884 23.534;
        25.925 22.857 26.241 28.675;
        24.001 33.768 27.689 24.99];
%-------------------------------------
% t-distribution values
t18 = 2.306;    % for 9 values
t24a = 2.365;   % for 8 values
```

```
t24b = 3.182;   % for 4 values
t36 = 3.182;    % for 4 values
%-------------------------------------
% P_i values
for j = 1:2
    P182a(j) = std(L182a(j,:))/sqrt(length(L182a(j,:)));
    P182b(j) = std(L182b(j,:))/sqrt(length(L182b(j,:)));
end
P182 = [P182a P182b];
clear P182a P182b
for i = 1:4
    P187(i) = std(L187(i,:))/sqrt(length(L187(i,:)));
    P181(i) = std(L181(i,:))/sqrt(length(L181(i,:)));
    P241(i) = std(L241(i,:))/sqrt(length(L241(i,:)));
    P242(i) = std(L242(i,:))/sqrt(length(L242(i,:)));
    P361(i) = std(L361(i,:))/sqrt(length(L361(i,:)));
    P362(i) = std(L362(i,:))/sqrt(length(L362(i,:)));
end
%-------------------------------------------------
% uncertainty of measured scatter
S187 = sqrt(P187(1)^2+P187(2)^2+P187(3)^2+P187(4)^2);
S181 = sqrt(P181(1)^2+P181(2)^2+P181(3)^2+P181(4)^2);
S182 = sqrt(P182(1)^2+P182(2)^2+P182(3)^2+P182(4)^2);
S241 = sqrt(P241(1)^2+P241(2)^2+P241(3)^2+P241(4)^2);
S242 = sqrt(P242(1)^2+P242(2)^2+P242(3)^2+P242(4)^2);
S361 = sqrt(P361(1)^2+P361(2)^2+P361(3)^2+P361(4)^2);
S362 = sqrt(P362(1)^2+P362(2)^2+P362(3)^2+P362(4)^2);
%-------------------------------------------------------------
% differential Pixel lengths
x187 = L187./25.02;
```

```
x181 = L181./25.02;
x182a = L182a./25.02;
x182b = L182b./20.7;
x182 = [x182a;x182b];
x241 = L241./19.5;
x242 = L242./19.5;
x361 = L361./19.25;
x362 = L362./19.25;
% uncertainty of pixel choice
for i = 1:4
    B187(i) = sqrt(x187(i,1)^2+x187(i,2)^2+x187(i,3)^2+...
     x187(i,4)^2+x187(i,5)^2+x187(i,6)^2+x187(i,7)^2+...
x187(i,8)^2+x187(i,9)^2);
    B181(i) = sqrt(x181(i,1)^2+x181(i,2)^2+x181(i,3)^2+...
     x181(i,4)^2+x181(i,5)^2+x181(i,6)^2+x181(i,7)^2+...
x181(i,8)^2+x181(i,9)^2);
    B182(i) = sqrt(x182(i,1)^2+x182(i,2)^2+x182(i,3)^2+...
     x182(i,4)^2+x182(i,5)^2+x182(i,6)^2+x182(i,7)^2+...
x182(i,8)^2+x182(i,9)^2);
    B241(i) = sqrt(x241(i,1)^2+x241(i,2)^2+x241(i,3)^2+...
     x241(i,4)^2+x241(i,5)^2+x241(i,6)^2+x241(i,7)^2+x241(i,8)^2);
    B242(i) = sqrt(x242(i,1)^2+x242(i,2)^2+x242(i,3)^2+x242(i,4)^2);
    B361(i) = sqrt(x361(i,1)^2+x361(i,2)^2+x361(i,3)^2+x361(i,4)^2);
    B362(i) = sqrt(x362(i,1)^2+x362(i,2)^2+x362(i,3)^2+x362(i,4)^2);
end
%-----------------------------------------------------------------
% average lengths
m182a = mean(L182a,2);
m182b = mean(L182b,2);
```

```
m187 = mean(L187,2);
m181 = mean(L181,2);
m182 = [m182a; m182b];
m241 = mean(L241,2);
m242 = mean(L242,2);
m361 = mean(L361,2);
m362 = mean(L362,2);

% TOTAL uncertainty of each set of parameters
for k = 1:4
    M(1,:) = m187;
    M(2,:) = m181;
    M(3,:) = m182;
    M(4,:) = m241;
    M(5,:) = m242;
    M(6,:) = m361;
    M(7,:) = m362;

    U(1,k) = sqrt(B187(k)^2 + t18*P187(k)^2);
    U(2,k) = sqrt(B181(k)^2 + t18*P181(k)^2);
    U(3,k) = sqrt(B182(k)^2 + t18*P182(k)^2);
    U(4,k) = sqrt(B241(k)^2 + t24a*P241(k)^2);
    U(5,k) = sqrt(B242(k)^2 + t24b*P242(k)^2);
    U(6,k) = sqrt(B361(k)^2 + t36*P361(k)^2);
    U(7,k) = sqrt(B362(k)^2 + t36*P362(k)^2);
end
%-----------------------------------------------
% Create a figure
X = [17.2 20.7 24.1 27.6];
```

```
figure
hold on
errorbar(X,M(1,:),U(1,:),'-.^k','MarkerFaceColor','k','MarkerSize',8)
errorbar(X,M(2,:),U(2,:),'-^k','MarkerFaceColor','c',...
'MarkerSize',8,'MarkerEdgeColor','k')
errorbar(X,M(3,:),U(3,:),'--^r','MarkerFaceColor','r',...
'MarkerSize',8,'MarkerEdgeColor','k')
errorbar(X,M(4,:),U(4,:),'-sk','MarkerFaceColor','c',...
'MarkerSize',8,'MarkerEdgeColor','k')
errorbar(X,M(5,:),U(5,:),'--sr','MarkerFaceColor','r',...
'MarkerSize',8,'MarkerEdgeColor','k')
errorbar(X,M(6,:),U(6,:),'-ok','MarkerFaceColor','c',...
'MarkerSize',8,'MarkerEdgeColor','k')
errorbar(X,M(7,:),U(7,:),'--or','MarkerFaceColor','r',...
'MarkerSize',8,'MarkerEdgeColor','k')
hold off
xlabel('Pressure [MPa]')
ylabel('Propagation Distance [cm]')
legend('0.46m-0.7mm','0.46m-1mm','0.46m-2mm',...
'0.61m-1mm','0.61m-2mm','0.91m-1mm','0.91m-2mm','Location','EastOutside')
print('-depsc','-tiff','-r1200','Length_Feb17')
```

A.2.3 Cloud Area

Significant image processing was required to convert the images into binary images without losing important data. This code measures the area of the cavitation cloud.

```
% Michael Wright
% Cavitating Submerged Water Jet
% 10/19/2011
% This program outlines the cavitation cloud in an image of a submerged
```

```
% cavitating water jet.
tic
clc;
clear all;
% Create [NxMxj] 3D array where each image is [NxMx1]
% Create list of files into an array
fiLes = dir('/Volumes/WRIGHTDRIVE/Supercav_BYU/JET/...
Images/Images18/2mm/3000_1/*.tif');
% Add the new directory to the path being searched
newpath = '/Volumes/WRIGHTDRIVE/Supercav_BYU/JET/...
Images/Images18/2mm/3000_1/';
addpath(newpath)

nozzle = imread(fiLes(1).name); % Read in first image to remove nozzle
background = imopen(nozzle,strel('disk',5));
nozzle2 = nozzle + background;
level = graythresh(nozzle2);%-0.5;
Bnoz = im2bw(nozzle2,level);
Bnoz = bwareaopen(Bnoz,30);
Wnoz = imcomplement(Bnoz);
X = ones(7);
Nozzle = imdilate(Wnoz,X);
%%
i = 1780;
k = 1780;%numel(fiLes)-20;
for j = i:k%numel(fiLes)
    iMage = imread(fiLes(j).name);   % Read each image to a 3D array iMage

    % Open image and use structuring element to turn the background blank
    background = imopen(iMage,strel('disk',5));
```

```
iMage2 = iMage + background;

% Convert the image to binary--black jet on white background
level = graythresh(iMage2)-0.35;
Bjet = im2bw(iMage2,level);
Bjet = bwareaopen(Bjet,30);

% Switch black/white of binary image
Wjet = imcomplement(Bjet);

% use first image to eliminate nozzle from subsequent images
WJn = Wjet-Nozzle;   % White jet without nozzle
for p = 1:128
    for q = 200:768
        if WJn(p,q) < 0
            WJn(p,q) = 0;
        end
    end
end
figure     % Show jet without the nozzle
imshow(WJn,'InitialMagnification',200);
pause(0.1)

% Plot the boundaries around each cloud
[B,L,N,A] = bwboundaries(WJn);
hold on
for m = 1:length(B)
    boundary = B{m};
    plot(boundary(:,2),boundary(:,1),'r','LineWidth',2)
    pause(0.1)
```

```
    end
    hold off
    % Computes the area of the jet in pixels
    Area(j) = bwarea(WJn);
end
%Find the average cloud area in square centimeters
Cloud = 0.0016.*Area(1,i:k);
C = [min(Cloud) max(Cloud) mean(Cloud) std(Cloud)];
```

A.2.4 Pulsation Frequency

The following code measures the image color intensity of a column of pixels at a fixed distance downstream from the nozzle. These intensity values are run through the fft function to find the frequency spectrum of the jets.

```
tic
clc;
clear all;
% Create [NxMxj] 3D array where each image is [NxMx1]
% Create list of files into an array
fiLes = dir('/Volumes/WRIGHTDRIVE/Supercav_BYU/JET/Images/...
Images18/1mm/3000_1/*.tif');
% Add the new directory to the path being searched
newpath = '/Volumes/WRIGHTDRIVE/Supercav_BYU/JET/Images/...
Images18/1mm/3000_1/';
addpath(newpath)
%%
i = 1;
clear Inten
for j = 10+50:numel(fiLes)-90     %change  beginning point for each set
    iMage = imread(fiLes(j).name);
```

```
    iCol = iMage(:,620);
    Inten(i) = sum(iCol)/length(iCol);
    i = i+1;
end

Fs = 5000;
y = [Inten, Inten, Inten];
Nsamps = length(y);
t = (1/Fs)*(1:Nsamps);
y_fft = abs(fft(y));
y_fft(1) = [];
y_fft = y_fft(1:Nsamps/2);
f = Fs*(0:Nsamps/2-1)/Nsamps;

figure(2)
plot(t,y)
xlabel('Time [s]')
ylabel('Intensity')
% print('-depsc','-tiff','-r1200','Intensity')
figure(3)
plot(f,y_fft)
xlabel('Frequency [Hz]')
ylabel('Magnitude')
% print('-depsc','-tiff','-r1200','FreqSpectrum')
%=========================================================
% frequency values from "Frequency.m" amplitude spectrum
clc
clear all

% all 18 inch data
```

```
s18_07 = [10 39 120 33 116 15 21 41 116,...
 113 686 790 31 77 113 750 851 882 954 1103 24...
  80 118 760 915, 16 114 781 114 750 56 427 678...
   754 830, 17 115 582 663 721 888 113 664 713...
    835 924 105 713 922];
t18_07 = 0.0068977573.*[2500 2500 2500 2500 2500...
 2500 2500 2500 2500, 3000 3000 3000 3000...
  3000 3000 3000 3000 3000 3000 3000 3000...
   3000 3000 3000 3000, 3500 3500 3500 3500...
    3500 3500 3500 3500 3500 3500, 4000 4000...
     4000 4000 4000 4000 4000 4000 4000 4000...
      4000 4000 4000 4000];

s18_1 = [115 627 663 692 907 116 616 637 665 918 115 536 692 821,...
 110 561 627 112 544 581 678 114 491 582, 111 577 112 533...
  589 740 32 112 583 640 1078, 42 109 233 543 643 810 467...
   519 570 778 115 460 550 788];
t18_1 = 0.0068977573.*[2500 2500 2500 2500 2500 2500 2500 2500...
  2500 2500 2500 2500 2500 2500, 3000 3000 3000 3000 3000 3000...
   3000 3000 3000 3000, 3500 3500 3500 3500 3500 3500 3500 3500...
    3500 3500 3500, 4000 4000 4000 4000 4000 4000 4000 4000 4000...
     4000 4000 4000 4000 4000];

s18_2 = [111 269 491 313 411 609 370 440 511 660, 94 280 317...
 392 332 410 723 18 308 453 490 634, 26 230 536 24 500 23 711,...
  40 402 522 582 51 278 353 429 41 226 288 350];
t18_2 = 0.0068977573.*[2500 2500 2500 2500 2500 2500 2500 2500...
 2500 2500, 3000 3000 3000 3000 3000 3000 3000 3000 3000...
  3000 3000 3000, 3500 3500 3500 3500 3500 3500 3500,...
   4000 4000 4000 4000 4000 4000 4000 4000 4000 4000 4000 4000];
```

```
% all 24 inch data
s24_1 = [35 120 580 689 629 706 788, 120 550 598 638 118 580...
 630 654 720, 118 475 580 685 118 464 542 613, 520 606...
  120 404 566 627];
t24_1 = 0.0068977573.*[2500 2500 2500 2500 2500 2500 2500,...
 3000 3000 3000 3000 3000 3000 3000 3000 3000, 3500 3500...
  3500 3500 3500 3500 3500 3500, 4000 4000 4000 4000 4000 4000];

s24_2 = [115 398 620, 473 510 883, 312 393, 380 512];
t24_2 = 0.0068977573.*[2500 2500 2500,...
 3000 3000 3000, 3500 3500, 4000 4000];

% all 36 inch data
s36_1 = [118 469 610 649 747, 117 530 649,...
 118 470 508 618 803, 119 560 797];
t36_1 = 0.0068977573.*[2500 2500 2500 2500 2500,...
 3000 3000 3000, 3500 3500 3500 3500 3500,...
 4000 4000 4000];

s36_2 = [392 427 479, 346 483 562, 282 365, 325 421 111];
t36_2 = 0.0068977573.*[2500 2500 2500, 3000 3000 3000,...
 3500 3500, 4000 4000 4000];

% shape denotes pipe length, color denotes nozzle
figure(1)
hold on
plot(t18_07,s18_07,'k^','MarkerSize',8,'MarkerFaceColor','k',...
'MarkerEdgeColor','k')
plot(t18_1,s18_1,'k^','MarkerSize',8,'MarkerFaceColor','c',...
'MarkerEdgeColor','k')
```

```
plot(t18_2,s18_2,'r^','MarkerSize',8,'MarkerFaceColor','r',...
'MarkerEdgeColor','k')
plot(t24_1,s24_1,'ks','MarkerSize',8,'MarkerFaceColor','c',...
'MarkerEdgeColor','k')
plot(t24_2,s24_2,'rs','MarkerSize',8,'MarkerFaceColor','r',...
'MarkerEdgeColor','k')
plot(t36_1,s36_1,'ko','MarkerSize',8,'MarkerFaceColor','c',...
'MarkerEdgeColor','k')
plot(t36_2,s36_2,'ro','MarkerSize',8,'MarkerFaceColor','r',...
'MarkerEdgeColor','k')
axis([16.1 28.6 0 1000])
ylabel('Frequency [Hz]')
xlabel('Pressure [MPa]')
legend('0.45m-0.7mm','0.45m-1mm','0.45m-2mm','0.61m-1mm',...
'0.61m-2mm','0.91m-1mm','0.91m-2mm','Location','EastOutside')
hold off
% print('-depsc','-tiff','-r1200','FrequencyPress')
```

A.2.5 Front Velocity Measurement

This code is similar to the length measurement, but it divides distances by the time between frames to find the velocity of the cloud front.

```
% Supercavitating Jet Measurements
% Michael Wright
% October 28, 2011
%
clc
clear all
```

```
% Create [NxMxj] 3D array where each image is [NxMx1]
% Create list of files into an array

 fiLes = dir('/Volumes/WRIGHTDRIVE/Supercav_BYU/JET/...
  Images/Images18/07mm/2500_1/*.tif');
 newpath = '/Volumes/WRIGHTDRIVE/Supercav_BYU/JET/...
  Images/Images18/07mm/2500_1/';

%-------------------------------------------------------------------------
addpath(newpath)
z = 3574
for j = 3398:3403
    imshow(fiLes(j).name);
    iMage(:,:,j) = imread(fiLes(j).name);   % Read each image to a 3D array
    imshow(iMage(:,:,j)) % Show image on the screen
    n = 1;                                  % Number of distances desired
    M(:,:,j) = ginput(2*n);                 % [X,Y,image #] of chosen points
    % Count the number of pixels between chosen points
    % In piXels each row contains the measurements from a single image
    for i = 1:n
        piXels(j,i) = sqrt((M(2*i,1,j)-M(2*i-1,1,j))^2 +...
          (M(2*i,2,j)-M(2*i-1,2,j))^2);
        % Conversion factor for each run:  pixels/m
          cFc = 2502;
          cFf = 2070;
          cF24 = 1950;
          cF36 = 1925;
    end
end
close all
```

```
piXels;
Length = piXels./cF24;    % Length of jet in cm
% Time between each frame
dT = 1/5000;
for m = 1:numel(Length)-1
    Velocity(m,1) = (Length(m+1) - Length(m))/dT; % Velocity in m/s
end
Velocity
%=========================================================
```

This code uses the values obtained from the previous to plot the velocities.

```
clc
clear all
%=========================================================================
% Velocity raw data where row is pressure
va725 = [43.89 57.911 32.15 57.945 58.078 57.935 53.762...
 73.938 44.007 47.993 33.965 32.011 33.828 34.089 47.97...
 1 37.968 33.993 85.875 62.126 49.831 30.011 63.983 41.997...
  43.944 57.968];
va730 = [41.955 69.933 39.995 27.973 83.924 79.991 47.956 65.908...
 50.015 75.898 61.807 57.944 65.975 71.855 79.87 69.965 75.927...
  85.924 79.918 72.009 80.079 43.884 49.9 64.203 53.955 50.059...
   83.933 78.033 59.877 71.991];
va735 = [87.981 61.977 77.86 87.895 73.956 77.92 72.037 75.92...
 64.024 74.001 76.042 83.875 76 74.07 51.938 71.958 47.945...
  63.956 65.994 49.906 50.052 79.932 55.954 49.977 67.927 66.01...
   71.925 75.958 87.901];
va740 = [84.084 59.695 54.075 43.843 51.964 72.059 73.922 57.909...
 63.924 53.975 51.991 71.916 65.962 77.986 75.911 61.976 40.114...
```

```
  79.958 49.948 71.878 76.015 85.949 71.782 64.016 49.953 79.909 67.886];

va125 = [97.873 85.937 87.938 65.97 79.927 77.932 81.87 86.001...
 85.891 65.97 67.915 75.956 75.896 83.956 81.96 45.943...
  55.969 47.928 62.093 61.956];
va130 = [75.952 63.931 81.989 43.923 56.003 77.882 59.991...
 59.947 69.96 83.931 57.972 43.962 83.91 73.945 95.913 81.934...
  65.965 79.928 83.933 67.936 76.083 69.844 81.951 79.931 93.91...
   93.931 92.04 71.859 73.961];
va135 = [89.879 77.8 79.935 69.854 85.982 101.87 63.949 81.939...
 85.927 85.882 79.935 59.952 51.958 91.916 109.93 55.95 99.92...
  83.999 77.931 99.92 89.942 53.956 67.94 79.951 66.022 83.956 81.887];
va140 = [101.97 51.881 55.951 61.954 95.939 95.899 99.924 93.941...
 85.909 79.994 111.82 51.994 65.96 79.918 77.941 83.933 101.92...
  93.96 83.907 103.92 107.92 73.985 97.889 93.921];

va225 = [64.005 56.033 53.862 50.032 60.075 63.881 73.807 61.947...
 61.906 59.947 67.901 71.902 59.951 77.933 55.959 77.962 89.808 67.945];
va230 = [65.945 45.956 49.966 81.978 71.91 69.925 61.95 83.936...
 73.937 71.959 75.775 73.939 94.12 81.779 93.977 89.849 74.03...
   81.856 81.928 61.942 71.845 93.924 125.9];
va235 = [57.964 55.577 89.371 79.709 108.8 79.639 96.188 77.375...
 99.033 94.236 94.179 101.49 57.917 67.64 31.4 53.139 43.478...
  55.572 94.184 65.227 82.146 101.57 67.491 74.947 65.149 48.308...
   91.833 94.155 79.71 79.706 72.478 74.868 79.719 58.065 77.274...
    55.51 86.957 65.248 55.552 96.63 79.708];
va240 = [62.898 55.442 55.564 65.216 86.978 103.86 87.015 74.837...
 113.6 96.597 128.02 135.25 96.618 94.227 77.278 103.85 53.139...
  65.216 60.386 123.19 94.203 106.26 106.32 106.26];
```

```
vb125 = [66.655 48.751 94.839 76.872 71.793 69.261 53.801 38.47...
 53.838 74.384 61.503 43.597 51.281 61.535 61.536 43.58 41.033...
  76.934 74.357 46.176];
vb130 = [64.101 74.409 46.096 71.793 74.351 71.818 69.199 53.846...
 41.031 64.102 79.483 79.511 61.511 105.12 76.921 87.178...
  69.229 61.557];
vb135 = [117.91 74.358 79.48 56.458 82.04 87.179 64.109 97.529 84.481...
 74.377 102.59 102.53 76.915 82.043 76.929 99.999 53.854...
  71.794 71.794 94.871];
vb140 = [46.134 64.102 41.025 135.85 97.436 89.749 115.38 79.414...
 61.635 51.191 110.28 87.156 102.56 64.273 74.155 105.12 84.601...
  82.051 59.088 107.63];

vb225 = [56.431 56.387 56.285 76.897 20.457 56.345 41.239 82.06...
 64.094 59 84.612 105.11];
vb230 = [84.553 58.974 56.415 69.266 79.475 56.35 79.534 61.58...
 61.496 46.221 77.051 58.911];
vb235 = [56.329 53.838 56.41 84.607 84.621 102.58 117.97 84.611...
 66.649 43.628];
vb240 = [84.578 79.544 105.15 94.837 64.101 76.921 76.979 69.224...
 84.57 87.175 79.549];

vc125 = [70.119 60.999 70.159 84.262 71.437 49.378 88.325 ...
72.714 92.406 64.752];
vc130 = [120.75 76.629 77.956 53.326 57.107 68.831 97.407 58.441];
vc135 = [89.61 66.236 67.556 97.388 80.528 93.498 90.994 75.254 92.196];
vc140 = [87.008 85.712 78.004 97.396 100.02 74.016 50.649 58.498 66.181];

vc225 = [72.698 73.772 69.113 68.659 58.416 71.431];
vc230 = [63.635 67.551 59.751 67.529 51.803 80.375 74.004 87.009...
```

```
 97.47 64.899 59.714];
vc235 = [67.504 76.629 74.019 97.499 89.733 76.878 46.764];
vc240 = [54.482 67.544 66.221 79.731 86.364 77.97 76.643 68.828 62.415];

%=========================================================================
P = [17.2 20.7 24.1 27.6];
M(1,:) = [mean(va725) mean(va730) mean(va735) mean(va740)];
M(2,:) = [mean(va125) mean(va130) mean(va135) mean(va140)];
M(3,:) = [mean(va225) mean(va230) mean(va235) mean(va240)];
M(4,:) = [mean(vb125) mean(vb130) mean(vb135) mean(vb140)];
M(5,:) = [mean(vb225) mean(vb230) mean(vb235) mean(vb240)];
M(6,:) = [mean(vc125) mean(vc130) mean(vc135) mean(vc140)];
M(7,:) = [mean(vc225) mean(vc230) mean(vc235) mean(vc240)];

pa7 = [2.06*std(va725)/length(va725) 2.04*std(va730)/length(va730)...
 2.04*std(va735)/length(va735) 2.06*std(va740)/length(va740)];
pa1 = [2.093*std(va125)/length(va125) 2.06*std(va130)/length(va130)...
 2.06*std(va135)/length(va135) 2.075*std(va140)/length(va140)];
pa2 = [2.11*std(va225)/length(va225) 2.08*std(va230)/length(va230)...
 2.021*std(va235)/length(va235) 2.07*std(va240)/length(va240)];
pb1 = [2.093*std(vb125)/length(vb125) 2.11*std(vb130)/length(vb130)...
 2.093*std(vb135)/length(vb135) 2.093*std(vb140)/length(vb140)];
pb2 = [2.201*std(vb225)/length(vb225) 2.201*std(vb230)/length(vb230)...
 2.262*std(vb235)/length(vb235) 2.228*std(vb240)/length(vb240)];
pc1 = [2.262*std(vc125)/length(vc125) 2.365*std(vc130)/length(vc130)...
 2.306*std(vc135)/length(vc135) 2.306*std(vc140)/length(vc140)];
pc2 = [2.571*std(vc225)/length(vc225) 2.228*std(vc230)/length(vc230)...
 2.447*std(vc235)/length(vc235) 2.306*std(vc240)/length(vc240)];

b = [0.506143459 0.670229957 0.559484344 ...
```

```
0.71395341 0.591797935 0.603702947 0.440279194;
0.726983035 0.807992835 0.756995585 0.772059922...
0.593313756 0.58239626 0.615818856;
0.760424639 0.84383483 1.197936383 0.964080439...
0.635963204 0.657790376 0.529531155;
0.688421238 0.854167381 1.097486477 0.99269112...
0.703865448 0.616505281 0.559002256];
B = b';

U(1,:) = [sqrt(B(1,1)^2 + pa7(1)^2) sqrt(B(1,2)^2 + pa7(2)^2)...
 sqrt(B(1,3)^2 + pa7(3)^2) sqrt(B(1,4)^2 + pa7(4)^2)];
U(2,:) = [sqrt(B(2,1)^2 + pa1(1)^2) sqrt(B(2,2)^2 + pa1(2)^2)...
 sqrt(B(2,3)^2 + pa1(3)^2) sqrt(B(2,4)^2 + pa1(4)^2)];
U(3,:) = [sqrt(B(3,1)^2 + pa2(1)^2) sqrt(B(3,2)^2 + pa2(2)^2)...
 sqrt(B(3,3)^2 + pa2(3)^2) sqrt(B(3,4)^2 + pa2(4)^2)];
U(4,:) = [sqrt(B(4,1)^2 + pb1(1)^2) sqrt(B(4,2)^2 + pb1(2)^2)...
 sqrt(B(4,3)^2 + pb1(3)^2) sqrt(B(4,4)^2 + pb1(4)^2)];
U(5,:) = [sqrt(B(5,1)^2 + pb2(1)^2) sqrt(B(5,2)^2 + pb2(2)^2)...
 sqrt(B(5,3)^2 + pb2(3)^2) sqrt(B(5,4)^2 + pb2(4)^2)];
U(6,:) = [sqrt(B(6,1)^2 + pc1(1)^2) sqrt(B(6,2)^2 + pc1(2)^2)...
 sqrt(B(6,3)^2 + pc1(3)^2) sqrt(B(6,4)^2 + pc1(4)^2)];
U(7,:) = [sqrt(B(7,1)^2 + pc2(1)^2) sqrt(B(7,2)^2 + pc2(2)^2)...
 sqrt(B(7,3)^2 + pc2(3)^2) sqrt(B(7,4)^2 + pc2(4)^2)];
%================================================================
figure(1)
hold on
errorbar(P,M(1,:),U(1,:),'-.^k','MarkerFaceColor','k','MarkerSize',8)
errorbar(P,M(2,:),U(2,:),'-^k','MarkerFaceColor','c',...
'MarkerSize',8,'MarkerEdgeColor','k')
errorbar(P,M(3,:),U(3,:),'--^r','MarkerFaceColor','r',...
```

```
'MarkerSize',8,'MarkerEdgeColor','k')
errorbar(P,M(4,:),U(4,:),'-sk','MarkerFaceColor','c',...
'MarkerSize',8,'MarkerEdgeColor','k')
errorbar(P,M(5,:),U(5,:),'--sr','MarkerFaceColor','r',...
'MarkerSize',8,'MarkerEdgeColor','k')
errorbar(P,M(6,:),U(6,:),'-ok','MarkerFaceColor','c',...
'MarkerSize',8,'MarkerEdgeColor','k')
errorbar(P,M(7,:),U(7,:),'--or','MarkerFaceColor','r',...
'MarkerSize',8,'MarkerEdgeColor','k')
hold off
xlabel('Pressure [MPa]')
ylabel('Pulse Velocity [m/s]')
legend('0.46m-0.7mm','0.46m-1mm','0.46m-2mm','0.61m-1mm',...
'0.61m-2mm','0.91m-1mm','0.91m-2mm','Location','Best')
% print('-depsc','-tiff','-r1200','Velocity_ALL')
```

A.2.6 Duration Measurements

This code plots the duration of the cavitation events.

```
clc
clear all
% Time chart for thesis
P = [17.2,20.7,24.1,27.6];
% row is nozzle, column is pressure, z is pipe
T(:,:,1) = [0.2197,0.2015,0.1930,0.1793;
            0.1521,0.1415,0.1330,0.1246;
            0.0471,0.0446,0.0435,0.0389];
T(:,:,2) = [0,0,0,0;
            0.1895,0.1627,0.1640,0.1557;
            0.0574,0.0536,0.0506,0.0490];
```

```
T(:,:,3) = [0,0,0,0;
            0.2586,0.2438,0.2334,0.2240;
            0.0824,0.0752,0.0734,0.0688];


figure(1)
hold on
%plot(P,T(1,:,1),'^k','MarkerFaceColor','k','MarkerSize',8)
plot(P,T(2,:,1),'-^k','MarkerFaceColor','c','MarkerSize',8,...
'MarkerEdgeColor','k')
plot(P,T(3,:,1),'--^r','MarkerFaceColor','r','MarkerSize',8,...
'MarkerEdgeColor','k')
plot(P,T(2,:,2),'-sk','MarkerFaceColor','c','MarkerSize',8,...
'MarkerEdgeColor','k')
plot(P,T(3,:,2),'--sr','MarkerFaceColor','r','MarkerSize',8,...
'MarkerEdgeColor','k')
plot(P,T(2,:,3),'-ok','MarkerFaceColor','c','MarkerSize',8,...
'MarkerEdgeColor','k')
plot(P,T(3,:,3),'--or','MarkerFaceColor','r','MarkerSize',8,...
'MarkerEdgeColor','k')
hold off
axis([16 28 0 0.28])
xlabel('Pressure [MPa]')
ylabel('Time of Jet [s]')
legend('0.46m-1mm','0.46m-2mm','0.61m-1mm','0.61m-2mm',...
'0.91m-1mm','0.91m-2mm','Location','EastOutside')
%print('-depsc','-tiff','-r1200','Time')
```